DOI 10.2478/ama-2025-0065

SLIPPAGE DOWN ON ROLLING MOBILE ROBOTS WHILE OVERCOMING INCLINED OBSTACLES

Jesús M. GARCÍA*, Franklyn G. DUARTE*

*Universidad Nacional Experimental del Táchira, Laboratory of Prototypes,
Universidad Street, Paramillo sector, San Cristóbal, Venezuela

jmgarcia@unet.edu.ve, fduarte@unet.edu.ve

received 27 January 2025, revised 09 September 2025, accepted 28 September 2025

Abstract: One of the challenges in terrestrial mobile robotics is the navigation of robots over uneven terrain composed of inclined surfaces and obstacles. During this task, the robot may tip over, get stuck, or slide down when moving on inclined surfaces. In this work, a novel metric is developed to predict the total slip risk of wheeled mobile robots when overcoming obstacles formed by inclined surfaces. This metric, called the slip index, was derived by analyzing friction forces, calculating instantaneous friction coefficients, and estimating the direction angle of the friction forces on each wheel, using an innovative approach. With this model, it will be possible to evaluate the robot's propensity to slip on inclined obstacles even before the robot moves over them, as long as certain geometric and physical characteristics of the obstacles are known beforehand. In this sense, the proposed index was validated through simulations and real-world tests, demonstrating efficient slip risk prediction with high accuracy, as evidenced by a low mean absolute percentage error (MAPE). This metric is a valuable tool for predicting imminent slip conditions, designing navigation strategies in uneven environments, and improving the robot's interaction with its surroundings.

Key words: friction force, slippage, slip index, instantaneous friction coefficients, navigability, overcoming obstacles

1. INTRODUCTION

Wheeled mobile robots (WMRs) have been widely used for outdoor navigation on terrains that are often irregular and full of obstacles. These robots are frequently employed in tasks such as exploration, military operations, search and rescue, agriculture, and planetary exploration. Some WMRs have specialized designs or use appropriate strategies to overcome obstacles. For instance, some possess passive suspension systems (spring-damper) that allow the wheels to pass over small obstacles [1-3]. Others use more elaborate passive suspension systems based on articulated links (e.g., the Rocker-bogie system) that allow the robots to progressively position their wheels over higher obstacles to overcome them [4]. In other cases, robots are equipped with active suspension systems, enabling the wheels to be positioned over obstacles with the help of actuators coupled to the suspension system [5].

In other innovative designs, the robot has an attached device that allows it to reposition its center of gravity, lifting its body and wheels, which can then be positioned over small obstacles with this action [6]. Other WMRs attach their wheels to rotational structures that, when facing an obstacle, rotate to position the wheels over the obstacles [7]. Similarly, some robots have legs with wheels attached as their end effectors. In this case, the robot moves by rolling with its wheels, but when it encounters an obstacle, it uses the legs to position the wheels over it [8].

Finally, some robots use additional support, either through some attached links [9] or arms that perform additional functions, but can also push against the ground, lifting the robot's body and wheels to position themselves over the obstacles to be overcome [10]. In all these cases, the study of the robot's obstacle-surmounting capability and its stability against tipping [11] have been a priority in studies conducted by researchers.

Furthermore, the study of friction and slippage has been another relevant topic in mobile robotics, as friction enables the rolling phenomenon to produce traction for wheeled and tracked robots. The study of friction began with the definition of different models for friction force [2,12], covering various topics including the characterization of slippage through parameters such as: the angle of lateral slippage that allows estimating the lateral displacement of the robot due to slippage, even when its speed is purely longitudinal [13,14], both on hard terrains and sandy terrains [15,16]. The percentage of slippage is also defined, which measures the relationship between the actual distance traveled by the robot including slippage and the ideal path [17]; and finally, longitudinal slippage which is measured in terms of the tangential speed of the wheels and the actual forward speed [18].

In the case of wheeled robots, it has been mentioned that the analysis of friction is vital as this force generates traction for the equipment's advancement. Regarding this, [19] indicates that, in a wheel, there are fundamentally two forces at the contact point of the wheel with the ground: firstly, the rolling resistance force R_i=$\mu_r\ N$ caused by non-elastic deformations of the wheel and the floor; this force is exerted in the opposite direction to the movement along the longitudinal axis of the wheel, although its direction may change during an ascent or descent movement of the wheel [20]. This force depends on the coefficient of rolling resistance (μ_r) and the normal force (N). If the wheel is considered rigid and the ground as well, this force can be neglected.

Secondly, the traction force (F_t) is exerted in the opposite

direction of slippage with orthogonal components F_{t_x} and F_{t_y}. As the name implies, this force generates traction for the wheel's advancement and depends fundamentally on the friction between the wheel and the ground; according to (1), these components can be obtained from the longitudinal (μ_x) and transversal (μ_y) friction coefficients along with the normal force (N).

$$F_t = \begin{bmatrix} F_{t_x} \\ F_{t_y} \end{bmatrix} = \begin{bmatrix} \mu_x N \\ \mu_y N \end{bmatrix} \quad (1)$$

Of course, the forces F_{t_x} and F_{t_y} can be used to obtain F_t through (2). Furthermore, in [21], a principle called the friction cone was used to indicate that F_t can always be considered proportional to N. From this, a single instantaneous friction coefficient ((μ_i) can be determined such that:

$$F_t = \sqrt{F_{t_x}^2 + F_{t_y}^2} = \mu_i N \quad (2)$$

Finally, it must always be ensured that $\mu_i \leq \mu_s$ (where μ_s is the static friction coefficient) to guarantee that the wheel does not experience total slippage, which can occur in the longitudinal or transversal direction. This analysis conducted on a single wheel can be extended to complete robots, but additional factors such as inertial and external forces must be considered, which may affect the necessary traction and grip forces to move the robot.

Therefore, it is necessary to carry out more comprehensive analyses on the entire robot to avoid or decrease the problem of total wheel slippage [22]. In this regard, other relevant and related aspects have been studied, such as: friction and slippage of robots on inclined surfaces [23], real-time determination of friction coefficient using sensors installed on the robot [9,24], terrain characterization based on the obtained friction coefficient and longitudinal slippage [25], influence of friction in defining trajectories and control systems to correct position deviations due to friction [26-28], torque control on the wheels to prevent slippage [2,29], power consumption in the robot considering friction [30], and finally, optimization of mobile robot performance by minimizing friction through possible improvements in geometry and active control of slippage and friction during driving [31].

Similarly, the topic of friction and slippage has been relevant for developing strategies that allow wheeled mobile robots to overcome obstacles. In this regard, friction force is considered a predominant element that must be leveraged to achieve effective obstacle traversal [32-34]. Multiple research studies have been conducted analyzing the limit condition to avoid slippage when wheeled mobile robots [35,36] or tracked robots [37] overcome step-like obstacles by utilizing friction as a traction force. Other research has carried out analogous work, deducing limit conditions to prevent slippage of tracked robots when ascending stairs [38,39].

All these analyses have been based on robots overcoming regular obstacles mainly formed by horizontal surfaces (steps or stairs), but little has been analyzed regarding the friction and slippage of robots when overcoming obstacles formed by inclined surfaces. Therefore, this work develops a metric that allows predicting the limit condition for total slippage when a wheeled robot is in the process of overcoming an obstacle formed by inclined surfaces. The specific case study is defined for Lázaro (Fig. 1), a robot that uses its arm as support to overcome the obstacle, but the metric can be extended to any wheeled robot that does not have or use its arm for this purpose. In this sense, the development of this normalized metric called Slip Index (I_s), including obtaining the instantaneous friction coefficients (μ_i) of the wheels in contact with each surface of the obstacle, and estimating the angle of the friction force in the plane of each surface (δ_n) constitute the main contributions of this work.

Fig. 1. Lázaro robot

The article is structured as follows: Section 2 deduces I_s based on the characterization of the obstacle and the robot, the analysis of the robot's reaction forces with the ground, the deduction of μ_i, and the estimation of δ_n. Section 3 presents and analyzes the results of applying various simulated experiments and real tests that have allowed validating the proposed metric and evaluating its effectiveness in predicting the possibility of total slippage while the robot overcomes an obstacle formed by inclined surfaces. Finally, in Section 4, conclusions are drawn and future work that can be developed from this research is outlined.

2. METHOD

2.1. Initial Assumptions

Initially, some guiding principles were defined that allowed delimiting and solving the problem considering some simplifications:

- The four contact points of the wheels with the ground are located in the same plane. This implies that both the suspension effect and the flexibility of the robot's parts are considered negligible.
- Each wheel's contact with the terrain is assumed to be point-like, with the understanding that the wheels and the ground are considered rigid.
- The overcoming process was defined according to a quasi-static analysis, which can be implemented when the robot and its manipulator move at low speeds and there are no large accelerations or inertial components apart from gravity, nor major external loads [40,41]. Therefore, the effect of dynamic loads was not considered.
- Prior characterization of the obstacle: basic geometric information of the obstacle will be necessary, which can be obtained from a characterization system, for example, using LiDAR [42].
- A friction analysis was conducted using the friction cone principle to determine the instantaneous friction coefficient ((μ_i).
- In practice, some important variables related to the robot's state (θ_1, d_2, α_c, ϕ_c) are always known through the sensor network installed on the robot.

DOI 10.2478/ama-2025-0065

2.1.1. Characterization of the Robot's Geometry

For this work, Lázaro [43] was used, which is a skid steer robot weighing *W=255.1 N*, with an attached arm that has two joints: a rotational one (θ_1) that moves the first link of the arm, and a prismatic one (d_2) that moves the second link of the arm (Fig. 2a). This arm is used in maneuvers to overcome obstacles and prevent tipping by acting as a counterweight or by placing its wheeled end-effector in contact with the ground. Additionally, it serves as a platform for installing sensors like a 2D rangefinder This allows the system to perceive its surroundings and more accurately detect and estimate obstacles. Subsequently, a frame fixed to the robot ($X_cY_cZ_c$) was defined, where the X_cY_c plane coincides with the plane containing the four contact points of the wheels with the ground, the X_c axis coincides with the longitudinal direction of the robot (forward motion), the Z_c axis is perpendicular to this plane, and its origin O_c is located at the intersection of the axis of the first joint in the robot's arm with the X_cY_c plane (Fig. 2a). The main dimensions of this robot are shown in Tab. 1.

Additionally, it is important to note that in Fig. 2b, $\Delta x_f = R_r sin(\phi_c - \phi_{s2})$ and $\Delta x_r = R_r sin(\phi_c - \phi_{s1})$, which correspond to variations in the position of the front and rear wheel contact points respectively (from the ideal position), occur when the wheels are positioned on surfaces that are not parallel to the X_cY_c plane. In this case, R_r is the radius of the wheels (the other variables will be defined later). Although this change in the wheel contact point position with the ground also induces a variation in the Z_c direction called Δz, it will be assumed negligible due to its small magnitude.

On the other hand, α_c and ϕ_c must be considered, which are the roll and pitch angles of the $X_cY_cZ_c$ frame with respect to a global frame $X_MY_MZ_M$ (to be defined later) and define the robot's inclination relative to a horizontal plane; these angles are obtained from an Inertial Measurement Unit (IMU) installed on the robot. With all the described variables, the position of the center of gravity and the weight vector (both defined according to the $X_cY_cZ_c$ frame) can be obtained for any inclination or position of the arm, through (3) and (4) respectively (Fig. 2a), where *a*, *b*, *c*, *d*, and *r* are constants specific to the robot.

$$\begin{bmatrix} W_x \\ W_y \\ W_z \end{bmatrix} = W \begin{bmatrix} \sin\phi_c \\ \cos\phi_c \sin\alpha_c \\ \cos\phi_c \cos\alpha_c \end{bmatrix} \tag{3}$$

$$\begin{bmatrix} x_{cog} \\ y_{cog} \\ z_{cog} \end{bmatrix} = \begin{bmatrix} a + r\cos\theta_1 \\ b + r\sin\theta_1 \\ c\ d_2 + d \end{bmatrix} \tag{4}$$

Tab. 1. Dimensional parameters of Lázaro robot

Parameter	Magnitude
x_f	209.0 mm
x_r	191.0 mm
x_t	400.0 mm
y_t	398.0 mm
a_1	420.0 mm
d_{2c}	- 282.5 mm

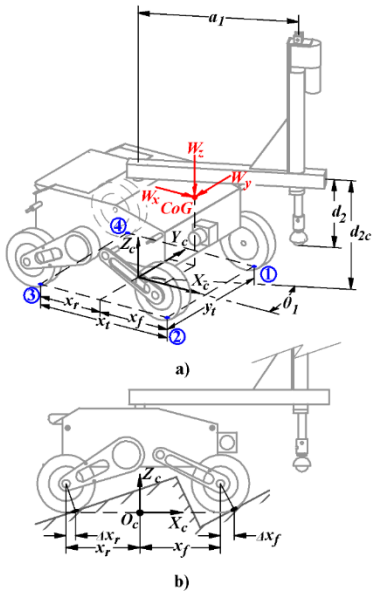

Fig. 2. Lázaro robot showing dimensions and $X_cY_cZ_c$ frame
a) Axono metric view; b) Side view

2.1.2. Characterization of the obstacle

According to the established premises, a simplified obstacle was defined as two flat surfaces: *Surface 1*, where the robot is located before overcoming the obstacle, and *Surface 2*, where the robot is located after overcoming the obstacle (Fig. 3). These surfaces are delimited by two edges considered straight lines: *Edge 1* delimits *Surface 1*, and *Edge 2* delimits *Surface 2*, so that the space between these edges defines the obstacle. Now, based on this, three frames were defined (Fig. 3):

- A fixed frame ($X_{s1}Y_{s1}Z_{s1}$), attached to *Surface 1*, where the $X_{s1}Y_{s1}$ plane is contained within *Surface 1*, the Z_{s1} axis is perpendicular to this surface, and the origin of this frame O_{s1} coincides with point O_c at an initial time instant ($t = 0$), when the robot has not yet started the obstacle overcoming process. At this instant, $X_{s1}Y_{s1}Z_{s1}$ coincides with $X_cY_cZ_c$.
- A fixed global frame ($X_MY_MZ_M$) where X_MY_M is located on a horizontal plane, the X_M axis coincides with the horizontal projection of X_{s1}, Z_M is vertical, and the origin O_M coincides with O_{s1}.
- A fixed frame ($X_{s2}Y_{s2}Z_{s2}$), attached to *Surface 2*, where the $X_{s2}Y_{s2}$ plane is contained within *Surface 2*, the Z_{s2} axis is perpendicular to this surface, the origin of this frame O_{s2} coincides with the intersection of *Edge 2* with the $X_{s1}Z_{s1}$ plane, and the X_{s2} axis coincides with the intersection of *Surface 2* with the $X_{s1}Z_{s1}$ plane.

Finally, the orientation of the $X_{s1}Y_{s1}Z_{s1}$ and $X_{s2}Y_{s2}Z_{s2}$ frames relative to the fixed frame $X_MY_MZ_M$ must be established using the *Roll* (α) and *Pitch* (ϕ) angles. Therefore, the following angles are defined:

- α_{s1}, ϕ_{s1}: *Roll* and *pitch* angles of the $X_{s1}Y_{s1}Z_{s1}$ frame relative to the $X_MY_MZ_M$ frame (define the inclination of *Surface 1* relative to horizontal plane).
- α_{s2}, ϕ_{s2}: *Roll* and *pitch* angles of the $X_{s2}Y_{s2}Z_{s2}$ frame relative to the $X_MY_MZ_M$ frame (define the inclination of *Surface 2* relative to horizontal plane).

Lastly, an angle called γ_{b1} is added, which measures the

inclination of *Edge 1* relative to the X_{s1} axis (or direction of robot advancement). All of these angles can be obtained using the IMU and a LiDAR (or arm with 2D rangefinder) installed on the robot.

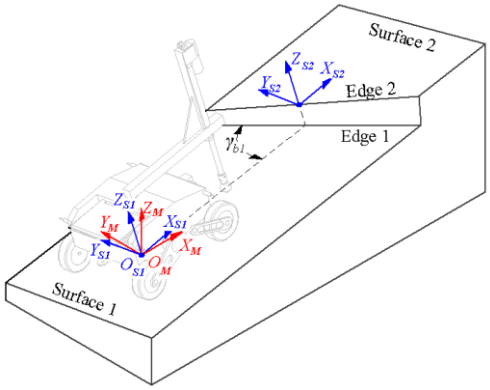

Fig. 3. Geometric parameters used to characterize the obstacle

2.2. Analysis of reaction forces

2.2.1. Dynamics of the contact between the robot's wheels and the ground

Let s be a surface where a wheel is positioned; this surface is defined through a frame $X_sY_sZ_s$ with its origin located at the wheel's contact point n $(n = 1 \dots 4)$ with the ground, the X_sY_s plane contained in surface s, the Z_s axis perpendicular to the surface, and the X_s axis in the rolling direction. With this, we can establish its pitch (ϕ_s) and roll (α_s) angles relative to a fixed frame $X_MY_MZ_M$ with the same origin as the $X_sY_sZ_s$ frame (Fig. 4a).

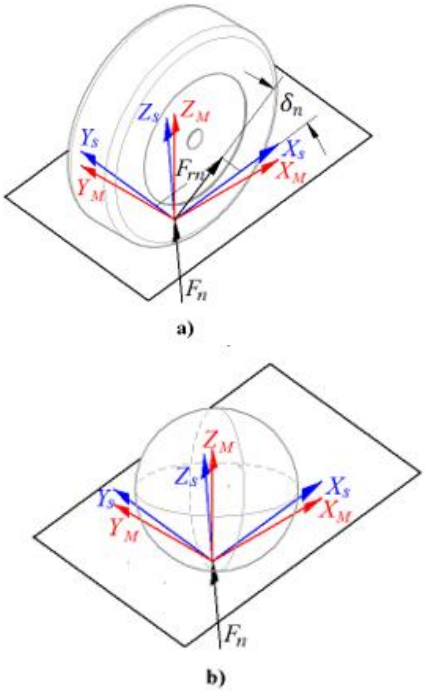

Fig. 4. Forces at the wheel-ground contact point: a) robot wheel; b) wheel at the end effector

If wheel n is in contact with surface s, a normal force F_n is produced along the Z_s axis, and a friction force F_{rn} is contained within the X_sY_s plane at an angle of inclination (δ_n) relative to the X_s axis. If the friction force $F_{rn} = \mu_i F_n$, where μ_i is the instantaneous coefficient of friction between the wheel and the ground, then the resulting force $\overrightarrow{{}^{s}F_{Tn}}$ at contact point n measured in the $X_sY_sZ_s$ frame is defined by:

$$\overrightarrow{{}^{s}F_{Tn}} = F_n \begin{bmatrix} \mu_i c\delta_n \\ \mu_i s\delta_n \\ 1 \end{bmatrix} \tag{5}$$

This force can be expressed in terms of $X_MY_MZ_M$ through (6):

$$\overrightarrow{{}^{M}F_{Tn}} = \begin{bmatrix} c\phi_s & s\phi_s s\alpha_s & s\phi_s c\alpha_s \\ 0 & c\alpha_s & -s\alpha_s \\ -s\phi_s & c\phi_s s\alpha_s & c\phi_s c\alpha_s \end{bmatrix} \overrightarrow{{}^{s}F_{Tn}} \tag{6}$$

Finally, $\overrightarrow{{}^{M}F_{Tn}}$ can be transformed using a frame parallel to the fixed frame of the robot $X_cY_cZ_c$ (with origin at the wheel-ground contact point), to obtain $\overrightarrow{{}^{c}F_{Tn}}$ through (7) with its components $[F_{nx} \quad F_{ny} \quad F_{nz}]^T$ defined by (8)-(10) in terms of the normal force F_n.

$$\overrightarrow{{}^{c}F_{Tn}} = \begin{bmatrix} F_{nx} \\ F_{ny} \\ F_{nz} \end{bmatrix} = \begin{bmatrix} c\phi_c & 0 & -s\phi_c \\ s\phi_c s\alpha_c & c\alpha_c & c\phi_c s\alpha_c \\ s\phi_c c\alpha_c & -s\alpha_c & c\phi_c c\alpha_c \end{bmatrix} \overrightarrow{{}^{M}F_{Tn}} \tag{7}$$

$$F_{nx} = F_n[c\phi_c(\mu_i c\phi_s c\delta_n + \mu_i s\phi_s s\alpha_s s\delta_n + s\phi_s c\alpha_s) - s\phi_c(-\mu_i s\phi_s c\delta_n + \mu_i c\phi_s s\alpha_s s\delta_n + c\phi_s c\alpha_s)] \tag{8}$$

$$F_{ny} = F_n[s\phi_c s\alpha_c(\mu_i c\phi_s c\delta_n + \mu_i s\phi_s s\alpha_s s\delta_n + s\phi_s c\alpha_s) + c\alpha_c(\mu_i c\alpha_s s\delta_n - s\alpha_s) + c\phi_c s\alpha_c(-\mu_i s\phi_s c\delta_n + \mu_i c\phi_s s\alpha_s s\delta_n + c\phi_s c\alpha_s)] \tag{9}$$

$$F_{nz} = F_n[s\phi_c c\alpha_c(\mu_i c\phi_s c\delta_n + \mu_i s\phi_s s\alpha_s s\delta_n + s\phi_s c\alpha_s) - s\alpha_c(\mu_i c\alpha_s s\delta_n - s\alpha_s) + c\phi_c c\alpha_c(-\mu_i s\phi_s c\delta_n + \mu_i c\phi_s s\alpha_s s\delta_n + c\phi_s c\alpha_s)] \tag{10}$$

2.2.2. Dynamics of the contact of the end effector wheel with the ground

The end effector of the arm installed on the Lázaro robot is a steerable wheel that, due to its characteristics, is considered omnidirectional. Therefore, the friction present occurs due to rolling effects; the magnitude of this friction is much lower than the sliding friction present in the other wheels of the robot. Therefore, for this wheel, friction is considered negligible, which implies that when this wheel touches the ground, it is only subjected to a normal force F_n (Fig. 4b). Thus, if we follow the procedure defined in the previous section but consider that μ_i=0, we can find equations (11)-(13) that define the projections of the normal force F_5 of this wheel with respect to the $X_cY_cZ_c$ frame. Finally, it is worth noting that the Lázaro robot has a resistive force sensor attached to the end effector, which allows estimating the magnitude of F_{5z}, from which the rest of the components can be estimated.

$$F_{5x} = F_5(c\phi_c s\phi_s c\alpha_s - s\phi_c c\phi_s c\alpha_s) \tag{11}$$

$$F_{5y} = F_5(s\phi_c s\alpha_c s\phi_s c\alpha_s - c\alpha_c s\alpha_s + c\phi_c s\alpha_c c\phi_s c\alpha_s) \tag{12}$$

$$F_{5z} = F_5(s\phi_c c\alpha_c s\phi_s c\alpha_s + s\alpha_c s\alpha_s + c\phi_c c\alpha_c c\phi_s c\alpha_s) \tag{13}$$

DOI 10.2478/ama-2025-0065

2.3. Analysis of Total Slippage Propensity

2.3.1. Slippage Index (I_s) Definition for Overcoming Obstacles

When a robot moves on an inclined surface, it can experience downhill slipping that may cause a deviation from its trajectory. In [23], a metric was developed to quantitatively estimate this risk in such cases. However, this metric is not useful when the robot is overcoming an obstacle because, in this scenario, the robot is positioned on two surfaces that may have different inclinations and properties. Therefore, it became imperative to develop a new metric in this case, which was defined based on the following premises:

- Although uncommon, the general case was considered where each surface may have its own static coefficient of friction (μ_s) when it is in contact with the robot's wheels. Therefore, μ_{s1} and μ_{s2} are the static coefficients of friction on *surfaces 1* and *2*, respectively.
- Each wheel has its own instant coefficient of friction (μ_i) with the ground. However, considering that the wheels on the same surface touch the same material (with identical properties), a single average instant coefficient of friction was assumed for the wheels touching a surface. Therefore, when the robot is overcoming an obstacle and its wheels touch two surfaces, μ_1 and μ_2 appear as the instant coefficients of friction of the wheels on *surfaces 1* and *2*, respectively.
- During the obstacle traversal, if a pair of wheels positioned on one surface starts to slip, they will immediately induce slippage in the other two wheels (positioned on the other surface); this indicates that slippage is not independent on each surface. Operationally, if slippage occurs when the instantaneous coefficient of friction (μ_i) equals the static coefficient of friction ($\mu_i = \mu_s$), both pairs of wheels simultaneously reach their respective μ_s if:

$$\frac{\mu_1}{\mu_2} = \frac{\mu_{s1}}{\mu_{s2}} \tag{14}$$

- When an individual element positioned on a surface starts to slip, it tends to move in the direction of maximum slope of the surface. However, this premise does not necessarily hold true in a complex system like a robot with multiple wheels, whose contacts are simultaneously distributed between two surfaces.
- The friction force on each wheel has an orientation angle δ_n with respect to the X_s axis. This angle depends mainly on the slope of the surface where the wheel is positioned and on the overall robot inclination; although it can also be affected by additional forces from other wheels and external disturbances. However, in this work, these additional influences were neglected, so it was considered that the wheels on the same surface will have the same δ_n, resulting in δ_1 and δ_2 corresponding to friction forces on *surfaces 1* and *2*, respectively.

Now, there is no slipping between two surfaces when $F_{s\,max} \geq F_s$, where F_s is the static friction force and $F_{s\,max}$ is the maximum static friction force. In the case of a wheel *n* touching a surface, $F_s = \mu_i F_n$, where F_n is the normal force; furthermore, $F_{s\,max} = \mu_s F_{n\,s}$, where $F_{n\,s}$ is the normal force calculated for the limit condition before slipping occurs. Therefore, the relationship $F_{s\,max} \geq F_s$ can be rewritten as:

$$\mu_s F_{n\,s} \geq \mu_i F_n \tag{15}$$

Additionally, if it is considered that when two wheels *n* and *m* are on the same surface, they have the same μ_s and μ_i, it can be stated according to (15) that:

$$\mu_s (F_m + F_n)_s \geq \mu_i (F_m + F_n) \tag{16}$$

Where $(F_m + F_n)_s$ is the sum of the normal forces belonging to wheels *m* and *n* calculated for the limit condition before slipping, while $(F_m + F_n)$ corresponds to the sum of these forces for an instantaneous condition with coefficient of friction μ_i. Based on this, a normalized slipping index I_s was defined by (17) whose magnitude is bounded between 1 and 0:1 for maximum grip with the ground and 0 for imminent slipping of the pair of wheels under study.

$$I_s = \frac{\mu_s (F_m + F_n)_s - \mu_i (F_m + F_n)}{\mu_s (F_m + F_n)_s} \tag{17}$$

Finally, if we consider that during obstacle overcoming the robot positions two wheels on each surface (Fig. 2b), an I_s can be defined for each surface (I_{s1}, I_{s2}), and a general index I_{sg} given by (18). This index allows evaluating the robot's propensity for slipping as a single system.

$$I_{sg} = \min(I_{s1}, I_{s2}) \tag{18}$$

Now, an analysis of the normal forces of wheels *m* and *n* was conducted in section 2.2.1, but the equations found include μ_i and δ_n, which are variables depending on the robot's instantaneous position at a given moment. These parameters are not directly obtained; therefore, in the following sections, an attempt is made to estimate these parameters.

2.3.2. Estimation of δ_n according to the obstacle's configuration

As previously mentioned, the orientation angle of the friction force on a wheel δ_n with respect to the X_s axis primarily depends on the inclination of the surface where the wheel is positioned, the inclination of the robot, and other factors already described that make its exact determination difficult, considering the robot as a system that has multiple δ_n but simplified to two in our case: one for each pair of wheels touching the same surface. Therefore, to initiate this study, the following angles shown in Fig. 5a were determined, which subsequently allow estimating δ_n depending on the system's conditions. These angles are:

- β_s: slope angle of surface *s* (maximum slope) relative to the X_s axis, defined in the $X_s Y_s Z_s$ frame.

$$\beta_s = \tan^{-1}\left(\frac{-\sin\alpha_s \cos\phi_s}{\sin\phi_s}\right) \tag{19}$$

- ε_s: slope angle opposite to the inclination of surface *s* (opposite to the maximum slope) relative to the X_s axis, defined in the $X_s Y_s Z_s$ frame.

$$\varepsilon_s = \tan^{-1}\left[\frac{\sin\alpha_s(\sin^2\phi_s + 1)}{-\cos\phi_s \sin\phi_s}\right] \tag{20}$$

- β_c: director angle of the robot's inclination (maximum slope of the $X_c Y_c$ plane) with respect to the X_M axis, defined in the $X_M Y_M Z_M$ frame.
- ε_c: angle opposite to the inclination of the robot (opposite to the maximum slope of the $X_c Y_c$ plane) with respect to the X_M axis, defined in the $X_M Y_M Z_M$ frame.

Although β_c and ε_c are defined in the $X_M Y_M Z_M$ frame, their projection can be found in the $X_s Y_s Z_s$ frame corresponding to the surface that the wheel touches (see Fig. 5b) through:

$$ {}^{s}\beta_c = \tan^{-1}\left(\frac{s\phi_s s\alpha_s s\phi_c c\alpha_c - c\alpha_s s\alpha_c}{c\phi_s s\phi_c c\alpha_c}\right) \quad (21) $$

$$ {}^{s}\varepsilon_c = \tan^{-1}\left(\frac{s\phi_s s\alpha_s s\phi_c c\alpha_c + c\alpha_s s\alpha_c}{-c\phi_s s\phi_c c\alpha_c}\right) \quad (22) $$

Once these angles were defined, a study was conducted based on multiple simulations carried out on a robot model in the MSC. ADAMS software that allowed studying δ_n and drawing some conclusions about it (associated with the angles defined previously). The results of these simulations are shown in Fig. 6, and from this, it can be stated that:

- When both surfaces are inclined in the same direction ($\beta_1 = \beta_2$), the robot slides in the direction of the maximum slope of these surfaces (see Fig. 6b, d, f, h), therefore, the friction force takes the opposite direction, such that $\delta_1 = \delta_2 = \varepsilon_s$.
- When one surface is horizontal, the friction of the wheels on that surface tends to take the direction of the friction of the other surface (see Fig. 6a, c, e, g), therefore $\delta_1 = \delta_2$.
- When both surfaces have a similar inclination ($|\beta_1 - \beta_2| \leq 90°$), the friction on the wheels on both surfaces tends to take the opposite direction to that shown by the maximum slope on each surface (see Fig. 6i, j, q, r). Therefore, it is assumed that $\delta_1 = \varepsilon_1$ and $\delta_2 = \varepsilon_2$.
- When both surfaces have a non-analogous inclination ($|\beta_1 - \beta_2| > 90°$, see Fig. 6k - p), the direction of the friction force tends to mostly follow the opposite direction of the maximum slope of the $X_c Y_c$ plane that defines the robot's inclination ($\delta_1 = {}^{s1}\varepsilon_c$ and $\delta_2 = {}^{s2}\varepsilon_c$), in situations where slipping is possible:
  - On surfaces resembling a concavity (see Fig. 6 m, o), this occurs if the surface facing the robot's natural sliding direction has a high inclination (HIS) while the other surface has a low inclination (LIS).
  - In the case of convex surfaces (see Fig. 6 k, n, p), this happens if the surface facing the robot's natural sliding direction has a low inclination (LIS) while the other surface has a higher inclination (HIS).

This rule is not absolute, as increasing the inclination of the surfaces, this configuration can change (see Fig. 6 l), and there can even be a wedge effect that limits the possibility of sliding.

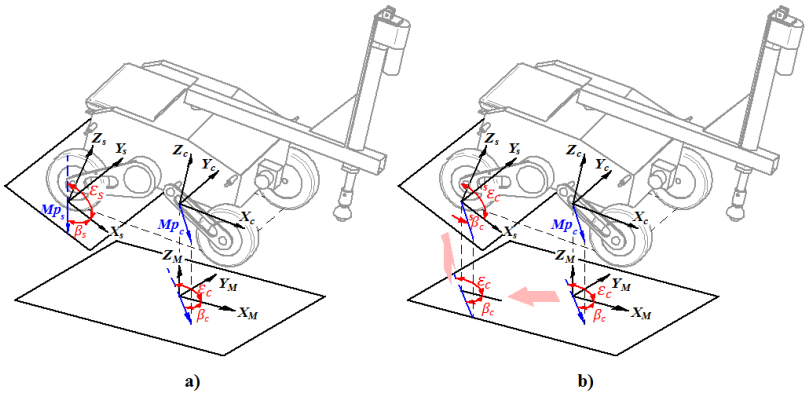

Fig. 5. Direct angles of the maximum slope on Surface s and on the $X_c Y_c$ plane

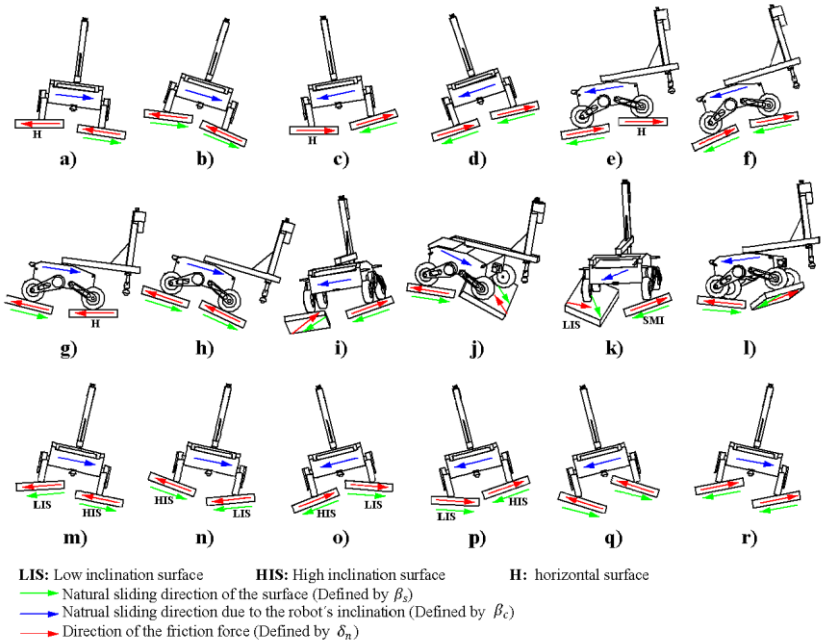

Fig. 6. Results of simulations to estimate δ_n

DOI 10.2478/ama-2025-0065

2.3.3. Determination of the instantaneous friction coefficient

Once the value of δ_n has been estimated in the previous section, this segment records a procedure for obtaining the instantaneous friction coefficient μ_i at the moment when the robot is overcoming the obstacle and has a pair of wheels positioned on each surface (see Fig. 7). This procedure is described separately for the case of overcoming the obstacle with the elevation of the front wheels (Fig. 7a) and overcoming with the side wheels (Fig. 7b).

Overcoming obstacles with front wheels: In this case, during the obstacle overcoming, the two front wheels are on *surface 2* while the two rear wheels are positioned on *surface 1*. The reaction forces of the 4 wheels represented in the $X_cY_cZ_c$ frame through their components F_{nx}, F_{ny} and F_{nz} (Fig. 7a) are obtained from (8)-(10). These equations include both the normal force F_n and the friction force (represented through μ_i and δ_n), of which F_n for each wheel and μ_i for each pair of wheels positioned on a surface are unknown. Therefore, these equations can be rewritten for the front wheels as:

$$F_{1x} = F_1(\mu_2 a + b) \quad F_{1y} = F_1(\mu_2 c + d)$$
$$F_{1z} = F_1(\mu_2 e + f) \tag{23}$$

$$F_{2x} = F_2(\mu_2 a + b) \quad F_{2y} = F_2(\mu_2 c + d)$$
$$F_{2z} = F_2(\mu_2 e + f) \tag{24}$$

Where μ_2 is the instantaneous friction coefficient of wheels 1 and 2 positioned on *surface 2*, and *a, b, c, d, e,* and *f* are process variables defined by (23).

$$\begin{cases} a = c\phi_c c\phi_{s2} c\delta_2 + c\phi_c s\phi_{s2} s\alpha_{s2} s\delta_2 + s\phi_c s\phi_{s2} c\delta_2 - s\phi_c c\phi_{s2} s\alpha_{s2} s\delta_2 \\ b = c\phi_c s\phi_{s2} c\alpha_{s2} - s\phi_c c\phi_{s2} c\alpha_{s2} \\ c = s\phi_c s\alpha_c c\phi_{s2} c\delta_2 + s\phi_c s\alpha_c s\phi_{s2} s\alpha_{s2} s\delta_2 + c\alpha_c c\alpha_{s2} s\delta_2 - c\phi_c s\alpha_c s\phi_{s2} c\delta_2 + c\phi_c s\alpha_c c\phi_{s2} s\alpha_{s2} s\delta_2 \\ d = s\phi_c s\alpha_c s\phi_{s2} c\alpha_{s2} - c\alpha_c s\alpha_{s2} + c\phi_c s\alpha_c c\phi_{s2} c\alpha_{s2} \\ e = s\phi_c c\alpha_c c\phi_{s2} c\delta_2 + s\phi_c c\alpha_c s\phi_{s2} s\alpha_{s2} s\delta_2 - s\alpha_c c\alpha_{s2} s\delta_2 - c\phi_c c\alpha_c s\phi_{s2} c\delta_2 + c\phi_c c\alpha_c c\phi_{s2} s\alpha_{s2} s\delta_2 \\ f = s\phi_c c\alpha_c s\phi_{s2} c\alpha_{s2} + s\alpha_c s\alpha_{s2} + c\phi_c c\alpha_c c\phi_{s2} c\alpha_{s2} \end{cases} \tag{23}$$

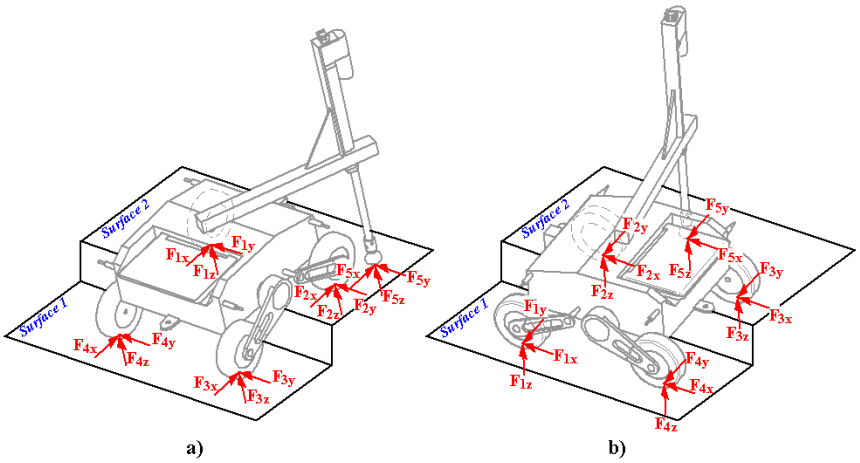

Fig. 7. Robot overcoming obstacle with two wheels on each surface

In the case of the rear wheels positioned on *surface 1*, the reaction forces are defined by:

$$F_{3x} = F_3(\mu_1 g + h) \quad F_{3y} = F_3(\mu_1 i + j)$$
$$F_{3z} = F_3(\mu_1 k + l) \tag{26}$$

$$F_{4x} = F_4(\mu_1 g + h) \quad F_{4y} = F_4(\mu_1 i + j)$$
$$F_{4z} = F_4(\mu_1 k + l) \tag{27}$$

Where μ_1 is the instantaneous friction coefficient of wheels 3 and 4 positioned on *surface 1*, and *g, h, i, j, k,* and *l* are process variables defined by (28).

$$\begin{cases} g = c\phi_c c\phi_{s1} c\delta_1 + c\phi_c s\phi_{s1} s\alpha_{s1} s\delta_1 + s\phi_c s\phi_{s1} c\delta_1 - s\phi_c c\phi_{s1} s\alpha_{s1} s\delta_1 \\ h = c\phi_c s\phi_{s1} c\alpha_{s1} - s\phi_c c\phi_{s1} c\alpha_{s1} \\ i = s\phi_c s\alpha_c c\phi_{s1} c\delta_1 + s\phi_c s\alpha_c s\phi_{s1} s\alpha_{s1} s\delta_1 + c\alpha_c c\alpha_{s1} s\delta_1 - c\phi_c s\alpha_c s\phi_{s1} c\delta_1 + c\phi_c s\alpha_c c\phi_{s1} s\alpha_{s1} s\delta_1 \\ j = s\phi_c s\alpha_c s\phi_{s1} c\alpha_{s1} - c\alpha_c s\alpha_{s1} + c\phi_c s\alpha_c c\phi_{s1} c\alpha_{s1} \\ k = s\phi_c c\alpha_c c\phi_{s1} c\delta_1 + s\phi_c c\alpha_c s\phi_{s1} s\alpha_{s1} s\delta_1 - s\alpha_c c\alpha_{s1} s\delta_1 - c\phi_c c\alpha_c s\phi_{s1} c\delta_1 + c\phi_c c\alpha_c c\phi_{s1} s\alpha_{s1} s\delta_1 \\ l = s\phi_c c\alpha_c s\phi_{s1} c\alpha_{s1} + s\alpha_c s\alpha_{s1} + c\phi_c c\alpha_c c\phi_{s1} c\alpha_{s1} \end{cases} \tag{28}$$

Next, static equilibrium operations were carried out using the second law of Newton (summation of forces and moments) with respect to the $X_cY_cZ_c$ frame, i.e., $\sum F_{Xc} = 0$, $\sum F_{Yc} = 0$, $\sum F_{Zc} = 0$ and $\sum M_{3-4} = 0$, to find the following system of equations with 4 unknowns $[(F_1 + F_2), (F_3 + F_4), \mu_1, \mu_2]$:

$$\begin{cases} (F_1 + F_2)(\mu_2 a + b) + (F_3 + F_4)(\mu_1 g + h) + m = 0 \\ (F_1 + F_2)(\mu_2 c + d) + (F_3 + F_4)(\mu_1 i + j) + n = 0 \\ (F_1 + F_2)(\mu_2 e + f) + (F_3 + F_4)(\mu_1 k + l) + o = 0 \\ (F_1 + F_2)(\mu_2 e + f)p + q = 0 \end{cases} \tag{29}$$

Where *m, n, o, p,* and *q* are process variables defined by:

$$\begin{cases} m = W_x - F_{5x} \\ n = F_{5y} - W_y \\ o = F_{5z} - W_z \\ p = x_t - \Delta x_r + \Delta x_f \\ q = F_{5z}(x_r - \Delta x_r + a_1 c\theta_1) \\ -F_{5x}(d_2 - d_{2c}) - W_z(x_r - \Delta x_r + x_{cog}) - W_x z_{cog} \end{cases} \quad (30)$$

Then, by algebraically manipulating the system given in (29), the following can be found:

$$F_1 + F_2 = \frac{-q}{p(\mu_2 e + f)} \quad (31)$$

$$F_3 + F_4 = \frac{q - op}{p(\mu_1 k + l)} \quad (32)$$

$$r\mu_1 + s\mu_1\mu_2 + t\mu_2 + v = 0 \quad (33)$$

Where *r, s, t,* and *v* are process variables such that:

$$\begin{cases} r = -qk(b+d) + f(q-op)(g+i) + pfk(m+n) \\ s = -qk(a+c) + e(q-op)(g+i) + pek(m+n) \\ t = -ql(a+c) + e(q-op)(h+j) + pel(m+n) \\ v = -ql(b+d) + f(q-op)(h+j) + pfl(m+n) \end{cases} \quad (34)$$

Finally, knowing that μ_1 and μ_2 are theoretically related through (14), we can solve for μ_2 to find that:

$$\mu_2 = \frac{-(r\mu_{s1} + t\mu_{s2}) \pm \sqrt{(r\mu_{s1} + t\mu_{s2})^2 - 4sv\mu_{s1}\mu_{s2}}}{2s\mu_{s1}} \quad (35)$$

If $\mu_2 \geq \mu_{s2}$, then $\mu_2 = \mu_{s2}$ so that slipping is imminent ($I_s = 0$). Finally, knowing μ_2, we can find μ_1 through (14), $F_1 + F_2$ from (31) and $F_3 + F_4$ from (32), which are necessary to determine the slipping index in each wheel pair given by (17). Additionally, $((F_1 + F_2)_s$ and $(F_3 + F_4)_s$ can be obtained from (31) and (32) respectively by substituting μ_1 with μ_{1s} and μ_2 with μ_{2s}.

For obstacle traversal with lateral wheels: In this case, during the obstacle traversal, the two wheels on the same side are on *surface 2* while the remaining two wheels are positioned on *surface 1* (Fig. 7b). The process to obtain the corresponding instantaneous friction coefficients for each surface (μ_1 and μ_2) along with the normal reaction forces ($F_n + F_m$) of each wheel pair is similar to that described for obstacle traversal with front wheels using equations (23)-(35), except that now the variables F_1 and F_2 (with their components) are replaced by the numbers of wheels on *surface 2*, while F_3 and F_4 (with their components) are replaced by the numbers of wheels on *surface 1*. After this, the entire process remains the same, including the process variables, except for *p* and *q*, which now take the following values:

$$\begin{cases} p = -y_t \\ q = -F_{5z}\left(\frac{y_t}{2} - a_1 s\theta_1\right) - F_{5y}(d_2 - d_{2c}) \\ \quad\quad + W_z\left(\frac{y_t}{2} - y_{cog}\right) + W_y z_{cog} \end{cases} \quad (36)$$

2.3.4. Analysis when the robot is supported by 2 wheels plus the end effector

This case occurs during certain stages of obstacle traversal when the robot is only supported by two wheels plus the end effector (Fig. 8). In this scenario, only two wheels provide sufficient grip to prevent slipping, so it is necessary to analyze them to determine their slip index (I_s). If the robot is supported by two wheels, *m* and *n*, and the weight components (W_x, W_y, W_z) are known, the normal force F_5 on the end effector can be determined according to the following cases:

- The front wheels are lifted ($F_1 + F_2 = 0$): F_5 is obtained through (37),
- The rear wheels are lifted (($F_3 + F_4 = 0$): F_5 is obtained through (38),
- The left-side wheels are lifted ($F_1 + F_4 = 0$): F_5 is obtained through (39),
- The right-side wheels are lifted ($F_2 + F_3 = 0$): F_5 is obtained through (40).

$$F_5 = \left[W_z(x_r - \Delta x_r + x_{cog}) + W_x z_{cog}\right] / \left[(x_r - \Delta x_r + a_1 c\theta_1)\,(s\phi_c c\alpha_c s\phi_s c\alpha_s + s\alpha_c s\alpha_s + c\phi_c c\alpha_c c\phi_s c\alpha_s) + (c\phi_c s\phi_s c\alpha_s - s\phi_c c\phi_s c\alpha_s)(d_2 - d_{2c})\right] \quad (37)$$

$$F_5 = \left[W_z(x_f + \Delta x_f - x_{cog}) - W_x z_{cog}\right] / \left[(x_f + \Delta x_f - a_1 c\theta_1)\,(s\phi_c c\alpha_c s\phi_{si} c\alpha_{si} + s\alpha_c s\alpha_{si} + c\phi_c c\alpha_c c\phi_{si} c\alpha_{si}) + (c\phi_c s\phi_{si} c\alpha_{si} - s\phi_c c\phi_{si} c\alpha_{si})(d_2 - d_{2c})\right] \quad (38)$$

$$F_5 = \left[W_z\left(\frac{y_t}{2} + y_{cog}\right) - W_y z_{cog}\right] / \left[\left(\frac{y_t}{2} + a_1 s\theta_1\right)(s\phi_c c\alpha_c s\phi_{si} c\alpha_{si} + s\alpha_c s\alpha_{si} + c\phi_c c\alpha_c c\phi_{si} c\alpha_{si}) - (s\phi_c s\alpha_c s\phi_{si} c\alpha_{si} - c\alpha_c s\alpha_{si} + c\phi_c s\alpha_c c\phi_{si} c\alpha_{si})(d_2 - d_{2c})\right] \quad (39)$$

$$F_5 = \left[W_z\left(\frac{y_t}{2} - y_{cog}\right) + W_y z_{cog}\right] / \left[\left(\frac{y_t}{2} - a_1 s\theta_1\right)(s\phi_c c\alpha_c s\phi_{si} c\alpha_{si} + s\alpha_c s\alpha_{si} + c\phi_c c\alpha_c c\phi_{si} c\alpha_{si}) + (s\phi_c s\alpha_c s\phi_{si} c\alpha_{si} - c\alpha_c s\alpha_{si} + c\phi_c s\alpha_c c\phi_{si} c\alpha_{si})(d_2 - d_{2c})\right] \quad (40)$$

After obtaining F_5, its components (F_{5x}, F_{5y}, F_{5z}) defined in the $X_c Y_c Z_c$ frame (see Fig. 8) can be derived using equations (11)-(13). Subsequently, the principles of the second law of Newton (sum of forces equals zero) according to the $X_c Y_c Z_c$ frame can be used to find the sum of reaction forces belonging to the two wheels touching the ground on the same surface:

$${}^c\vec{F}_{mn} = \begin{bmatrix} F_{mnx} \\ F_{mny} \\ F_{mnz} \end{bmatrix} = \begin{bmatrix} F_{mx} + F_{nx} \\ F_{my} + F_{ny} \\ F_{mz} + F_{nz} \end{bmatrix} = \begin{bmatrix} -(W_x + F_{5x}) \\ W_y - F_{5y} \\ W_z - F_{5z} \end{bmatrix} \quad (41)$$

Then, F_{mn} can be expressed in terms of the $X_M Y_M Z_M$ frame through (42) and subsequently, with respect to the $X_s Y_s Z_s$ frame corresponding to the surface where the two wheels are positioned, through (43):

$${}^M\vec{F}_{mn} = \begin{bmatrix} c\phi_c & s\phi_c s\alpha_c & s\phi_c c\alpha_c \\ 0 & c\alpha_c & -s\alpha_c \\ -s\phi_c & c\phi_c s\alpha_c & c\phi_c c\alpha_c \end{bmatrix} {}^c\vec{F}_{mn} \quad (42)$$

DOI 10.2478/ama-2025-0065

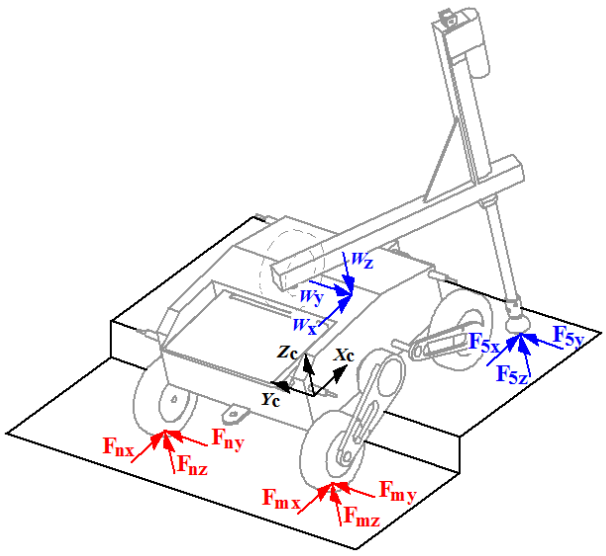

Fig. 8. Robot overcoming obstacle supported by 2 wheels and the end effector

$$ {}^{s}\vec{F}_{mn} = \begin{bmatrix} {}^{s}F_{mnx} \\ {}^{s}F_{mny} \\ {}^{s}F_{mnz} \end{bmatrix} = \begin{bmatrix} c\phi_s & 0 & -s\phi_s \\ s\phi_s s\alpha_s & c\alpha_s & c\phi_s s\alpha_s \\ s\phi_s c\alpha_s & -s\alpha_s & c\phi_s c\alpha_s \end{bmatrix} {}^{M}\vec{F}_{mn} \tag{43} $$

Finally, considering the assumptions made in this work: both wheels on the same surface have a single μ_i and δ_n, we can consider that the combined normal force between the two wheels is ${}^{s}F_{mnz}$, while the combined friction force is $\sqrt{{}^{s}F_{mnx}^2 + {}^{s}F_{mny}^2}$. Therefore, μ_i can be determined using (44) and δ_n using (45). With this information known, the sliding index I_s can be determined through (17) and it is also considered that the general index $I_{sg} = I_s$ since there is only sliding contact with one surface.

$$ \mu_i = \frac{\sqrt{{}^{s}F_{mnx}^2 + {}^{s}F_{mny}^2}}{{}^{s}F_{mnz}} \tag{44} $$

$$ \delta_n = \tan^{-1}\frac{{}^{s}F_{mny}}{{}^{s}F_{mnx}} \tag{45} $$

3. RESULTS AND DISCUSSION

3.1. Validation of I_s using MSC. ADAMS

To validate the proposed I_s, 6 tests were conducted using the robot model simulated in the MSC. ADAMS software. In each test, two wheels of the robot were placed on surface S_1 while the remaining two wheels were on surface S_2 (see Fig. 9); simultaneously, one of the two surfaces (S_1 or S_2) slowly rotated through a joint "A" to increase its inclination either in one direction (Fig. 9a, b, c, d) or in two directions (Fig. 9e, f). Each simulation was run until the robot lost grip with the ground and total sliding began. To complete the validation, in each of the 6 tests, 3 additional simulations were performed where the end effector of the arm was in contact with one of the two surfaces (S_1 or S_2), exerting a reaction force with magnitudes of 15, 30, and 45 N. In total, this validation consisted of 24 simulations.

On the other hand, to make the simulations more realistic, the characteristics of the contact between the wheels and the surfaces were methodically defined. Specifically, the MSC. ADAMS software uses the IMPACT function to define contact between two surfaces; in [44], it is indicated that this function is based on the Hertzian contact theory but considers the non-linear contact force $F_c = k(x_1 - x)^e$, where $(x_1 - x)$ is the depth of penetration during contact, e is the exponent of the force whose recommended magnitudes are listed in (46) and k is the static stiffness parameter defined through (47).

$$ e = \begin{cases} 2.2 & Hard\ materials\ like\ steel \\ 1.5 & Soft\ metals\ like\ aluminum \\ 1.1 & Very\ soft\ materials\ like\ rubber \end{cases} \tag{46} $$

$$ k = 2\left[\frac{3L\left(\frac{1}{R_{c1}}+\frac{1}{R_{c2}}\right)^{-1}}{4\left(\frac{1-\nu_1^2}{E_1}+\frac{1-\nu_2^2}{E_2}\right)^{-1}}\right]^{\frac{1}{3}}\left(\frac{1-\nu_1^2}{E_1}+\frac{1-\nu_2^2}{E_2}\right)^{-1} \tag{47} $$

Where L is the applied normal load (in this case $L \approx W/4$), R_{c1} and R_{c2} are the radii of curvature of the two contacting surfaces; E_1 and E_2 are the Young's modulus of the materials composing the contacting surfaces; and ν_1, ν_2 are the Poisson's ratios of the two materials in contact. For these simulations, it was considered that the robot has Polyethylene wheels and the surfaces S_1 and S_2 are made of concrete. Therefore, combining these two materials: $k = 3017.15\ N/mm^2$ and $e \approx 1.7$, these magnitudes were defined by [45]. Additionally, $(x_1 - x) = 0.01\ mm$ was used according to the recommendation given by [44]. On the other hand, the IMPACT function takes into account energy dissipation due to deformation; for this, ADAMS uses a parameter to create a damping force that dissipates energy from the system, the maximum magnitude of this parameter is defined as $C_{max} = 0.01k$. Therefore, in these simulations, $C = 30.17\ N/(mm.s)$ was used.

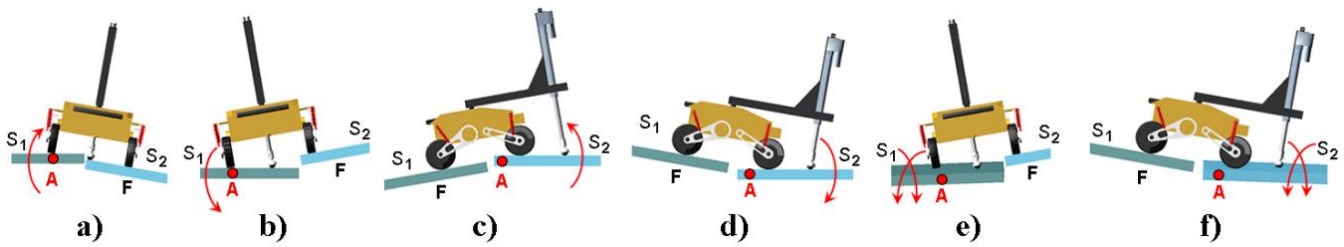

Fig. 9. Simulations to validate I_s with the robot touching the ground with 4 wheels

Additionally, to perform a realistic simulation, the effect of friction on the contacts between the wheels and surfaces must be considered. MSC. ADAMS uses the Coulomb friction model; therefore, for each contact, the static friction coefficient (μ_s) and dynamic friction coefficient (μ_k) must be defined, which depend on the materials in contact. Furthermore, the model used in this program does not allow for perfect contact without sliding; therefore, a "Stiction Velocity (V_s)" or maximum sliding velocity during static friction and a "Transition Velocity between Static and Dynamic Friction (V_d)" must be defined; V_d estimates the sliding during the transition phase between these two types of friction. For this work, $V_s = 50\ mm/s$ and $V_d = 60\ mm/s$ were defined, so that when the sliding velocity on a wheel is below $50\ mm/s$, the wheel will be under a regime of static friction (no real sliding), and when this velocity is above $60\ mm/s$, the wheel will experience total sliding.

The Fig. 10 shows the results obtained from conducting test "a" (according to Fig. 9) with F_{5z}=0 N. Specifically, in Fig. 10a, the reaction forces of the wheels with the ground are shown: $F_1 + F_4$, corresponding to the wheels on surface S_1; and $F_2 + F_3$, the equivalents on surface S_2. Additionally, Fig. 10b displays the instantaneous friction coefficients of the 4 wheels on their respective contact surface (μ_{r1}, μ_{r2}, μ_{r3} and μ_{r4}) and the combined friction coefficients between the two wheels in contact for surface S_1 ($\mu_1 = [\mu_{r1} + \mu_{r2}]/2$) and S_2 ($\mu_2 = [\mu_{r3} + \mu_{r4}]/2$). Both figures show the correspondence between the results obtained by the theoretical model and their equivalents achieved through simulation: it can be observed that the theoretical model predicts with a high degree of precision the real behavior of the reaction forces and friction coefficients as obtained through simulation: the percentage error obtained between the two analyses is: 1.99% and 1.19% for the reaction forces $F_1 + F_4$ and $F_2 + F_3$ respectively; furthermore, 0.80% and 3.42% for the friction coefficients μ_1 and μ_2.

On the other hand, Fig. 10c shows in the upper graph the sliding velocity V_s of each wheel, while the lower graph displays the slipping index I_s calculated with the proposed theoretical model. It can be observed that the slipping index reaches a value of 0 approximately at 3.1 seconds of simulation, indicating that at that moment, the robot should start slipping. This is evidenced by the fact that at the same instant, there is a change in the sliding velocity of each wheel (V_{s1}, V_{s2}, V_{s3} and V_{s4}), exceeding the threshold of $60\ mm/s$, indicating that the wheels have started slipping completely, and consequently, the robot. This analysis is valid for the rest of the tests conducted; for example, in Fig. 11, the results for a simulation corresponding to Test "d" (see Fig. 9) are shown, where the contact surfaces change configuration (the front wheels are on S_2 and the rear ones on S_1), in addition to F_{5z}=15 N. In this case, the correspondence of results between the theoretical model and the simulation is also show, along with the capability of I_s to estimate the exact moment when the slipping begins in the robot.

At this point, it is important to mention the results obtained in test "f" (see Fig. 9) where surface S_2 rotates descending in two directions. For this case, it was found that the robot loses contact of one wheel with the ground (evidenced by $\mu_{r2} = 0$ at 0.2 s in Fig. 12b), and additionally, it was observed that as F_{5z} increases, the theoretical model becomes less efficient in predicting the exact magnitude of instantaneous friction coefficients (see Fig. 12b) and the exact moment when slipping begins in the robot: in Fig. 12c, the wheels start slipping at 1.75 s while $I_s \approx 0.1$, which makes the prediction inaccurate in this case. This premise can be validated by studying Tab. 2, which presents the statistical analysis of all simulations conducted: the mean error ($\bar{\mu}$), standard deviation (σ), and mean absolute percentage error (*MAPE*) for the forces on surfaces S_1 (F_{S1}) and S_2 (F_{S2}), and the combined friction coefficients on the same surfaces (μ_1 and μ_2).

From that table, it is evident that the model becomes more inaccurate as the force F_{5z} increases, especially in cases where the surface moves in two directions (tests e and f). This inefficiency becomes more tangible in determining the combined friction coefficients where a maximum percentage error of 24.78% was reached (in only one simulation), while in other cases, it does not exceed 20%, which qualifies the model as having good forecasting ability according to [46]. However, knowing that in certain situations, a significant error can occur that directly affects the efficiency of the calculated I_s, it is recommended from a practical standpoint that at all times $I_s \geq 0.2$, which ensures safe movement without total slipping while overcoming obstacles.

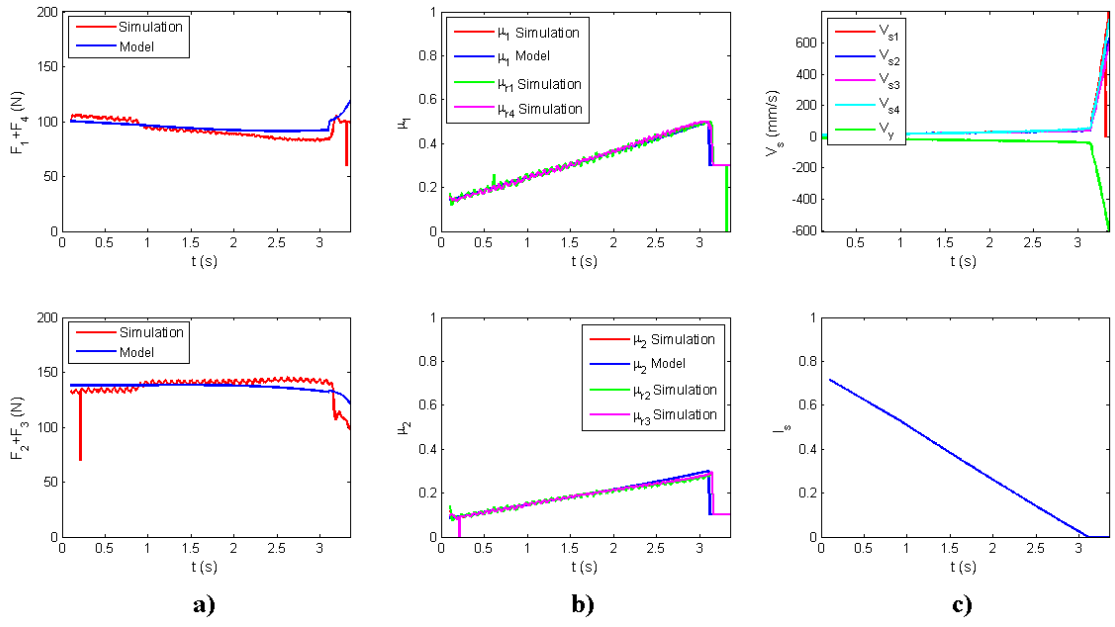

Fig. 10. Results corresponding to Test "a" (Fig. 9) with F_{5z}=0 N

DOI 10.2478/ama-2025-0065

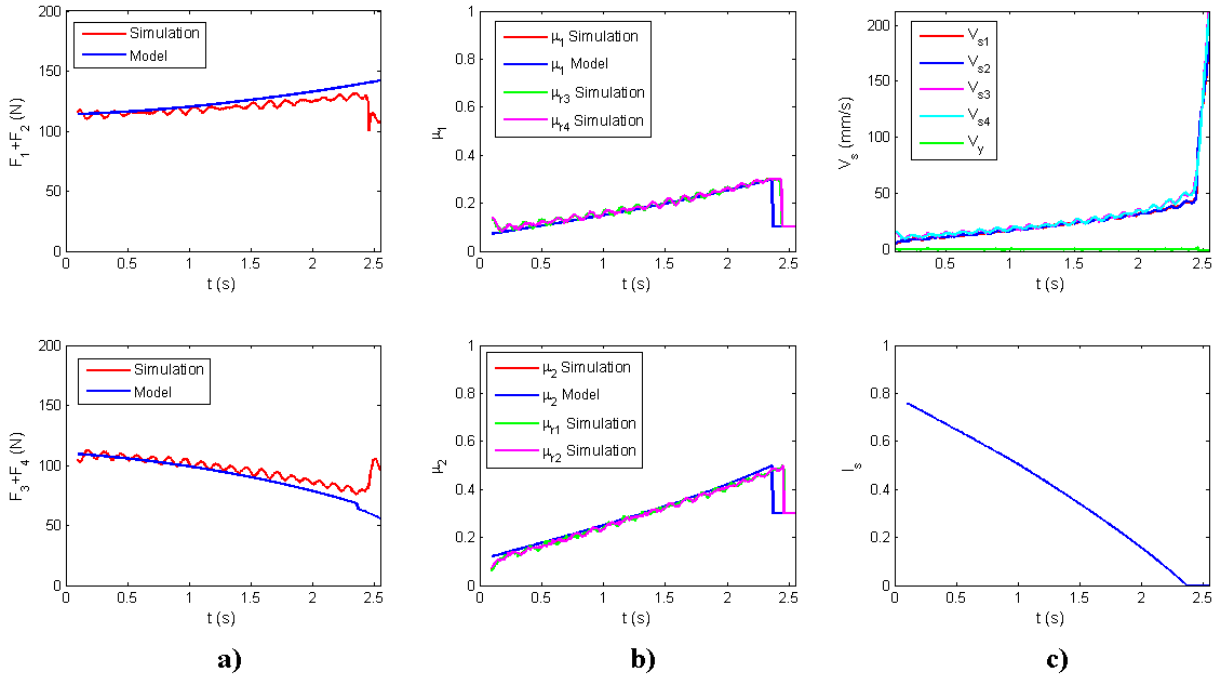

Fig. 11. Results corresponding to Test "d" (Fig. 9) with F_{5z}=15 N

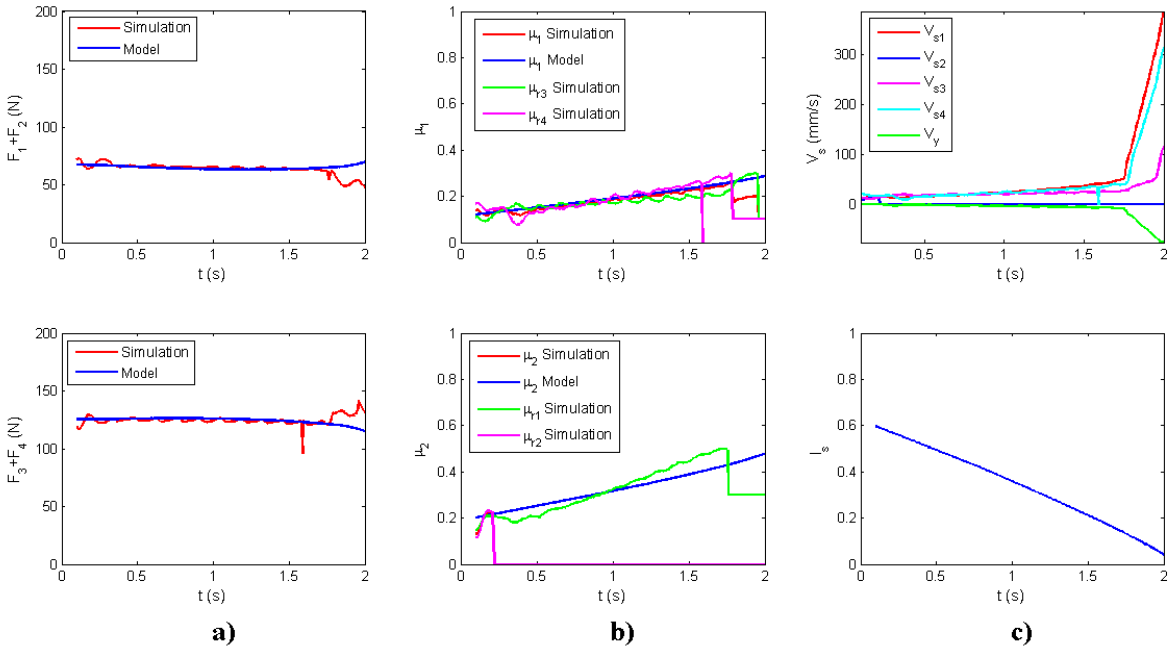

Fig. 12. Results corresponding to Test "f" (Fig. 9) with F_{5z}=45 N

Tab. 2. Statistical analysis of simulation results to validate l_s

Test	F_5 (N)	F_{s1}			F_{s2}			μ_1			μ_2		
		$\bar{\mu}$ (N)	σ (N)	$MAPE$ (%)	$\bar{\mu}$ (N)	σ (N)	$MAPE$ (%)	$\bar{\mu}$	σ	$MAPE$ (%)	$\bar{\mu}$	σ	$MAPE$ (%)
a	0	-2.01	4.61	1.99	1.68	6.22	1.19	0.00	0.01	0.80	-0.01	0.01	3.42
	15	-1.98	4.47	2.13	1.90	4.71	1.43	0.00	0.01	1.57	0.00	0.01	2.32
	30	-2.04	4.57	2.41	2.00	4.45	1.60	0.02	0.01	5.83	0.00	0.01	0.72
	45	-1.38	4.54	1.79	1.18	5.00	1.03	0.05	0.01	17.25	0.01	0.05	0.24
b	0	1.45	4.52	1.00	-1.95	4.63	2.02	0.00	0.00	0.41	0.00	0.01	1.08
	15	0.27	5.33	0.15	-0.66	5.79	0.75	0.00	0.03	2.25	0.00	0.04	4.53
	30	-1.75	5.52	1.47	1.45	6.11	1.73	0.00	0.03	0.37	-0.01	0.06	9.85
	45	-2.08	4.20	1.85	1.74	4.13	2.39	0.02	0.02	8.24	0.01	0.04	5.80

c	0	-7.54	7.56	5.16	7.09	6.31	7.50	0.00	0.04	2.27	-0.02	0.03	8.75
	15	-8.01	8.75	5.22	7.21	6.00	10.13	-0.01	0.05	3.21	-0.03	0.04	9.89
	30	-7.30	8.07	4.57	6.63	6.09	13.01	-0.01	0.05	6.60	-0.03	0.05	9.99
d	0	4.16	3.46	4.31	-4.47	2.88	3.10	0.01	0.01	3.56	-0.01	0.01	3.69
	15	3.80	3.61	3.61	-4.24	2.98	3.53	0.01	0.01	2.80	-0.01	0.01	3.72
	30	3.47	3.80	2.99	-4.03	3.90	4.25	0.01	0.01	2.15	-0.01	0.01	3.53
	45	3.35	4.25	2.71	-4.04	5.14	5.80	0.00	0.01	1.22	-0.01	0.01	3.93
e	0	-9.04	1.77	6.01	8.61	1.94	10.52	-0.01	0.02	4.50	0.05	0.01	5.44
	15	-9.13	1.78	6.44	9.03	1.50	11.73	-0.01	0.01	3.82	0.05	0.01	8.88
	30	-7.57	7.62	5.88	7.48	4.07	9.86	-0.02	0.06	24.78	0.04	0.01	15.52
	45	-8.15	2.08	6.77	8.14	2.58	11.61	0.00	0.01	0.45	0.04	0.06	17.69
f	0	3.35	4.66	3.24	-3.90	4.21	2.82	0.02	0.01	15.82	-0.02	0.03	6.28
	15	3.99	6.81	3.49	-4.48	6.66	3.95	0.02	0.01	14.91	-0.02	0.06	8.35
	30	1.32	5.69	0.99	-2.29	6.58	2.75	-0.02	0.04	12.12	-0.02	0.02	8.81
	45	0.77	5.85	0.53	-1.71	5.75	2.76	-0.02	0.03	10.13	-0.02	0.03	7.65

On the other hand, to validate Is when the robot is supported on 2 wheels plus the end effector, six additional simulations were conducted (see Fig. 13) where two wheels were supported on one surface (S1 or S2) while the end effector of the arm provided a third point of contact supported on the other surface. Similarly, a surface rotated through a joint "A" either in one direction (see Fig. 13a, b, c, and d) or in two directions (see Fig. 13e and f). It is worth noting that in this case, the magnitude of F5z depends on the system's own dynamics.

Fig. 14 shows the results obtained in test "b" (see Fig. 13). In this case, there is a greater fidelity of the model to estimate the magnitude of the contact forces of the wheels with the ground ($F_1 + F_2$, see Fig. 14a). This same accuracy in the model is observed when estimating the magnitude of the combined friction coefficient between the two wheels touching the surface (μ_1, see Fig. 14c); although using the model, μ_1 reaches its maximum magnitude (μ_s) before than in the simulation (in the model, this occurs at 1.45 s while in the simulation it occurs at 1.55 s). This also results in I_s reaching magnitude 0 at 1.45 s (Fig. 14d), while the robot actually starts to slide at 1.55 s (according to the change observed in the sliding speed V_s in Fig. 14b). This small difference (repeated in all simulations) is far from being detrimental; it allows I_s to predict the sliding promptly before it occurs.

Regarding this, Tab. 3 presents the statistical analysis of these simulations: the mean error ($\bar{\mu}$), standard deviation (σ), and mean absolute percentage error (*MAPE*) for the forces on surfaces S_1 (F_{S1}) or S_2 (F_{S2}), and the combined friction coefficients on the same surfaces (μ_1 or μ_2). In this case, the greater accuracy of the model is confirmed, as the absolute percentage error obtained is much lower: the maximum error found was 1.67% for the estimation of μ_2 in test "f". Based on this premise, it can be stated that the model provides a forecast of high precision, according to the criteria expressed by [46].

Tab. 3. Statistical analysis of the simulations when the robot touches the ground at 3 points

Test	F_{s1}			F_{s2}			μ_1			μ_2		
	$\bar{\mu}$ (N)	σ (N)	*MAPE* (%)	$\bar{\mu}$ (N)	σ (N)	*MAPE* (%)	$\bar{\mu}$	σ	*MAPE* (%)	$\bar{\mu}$	σ	*MAPE* (%)
a	0.15	4.10	0.06	-	-	-	0.01	0.04	0.98	-	-	-
b	-	-	-	0.21	1.53	0.17	-	-	-	0.01	0.05	1.53
c	-0.21	1.20	0.16	-	-	-	0.01	0.04	0.13	-	-	-
d	-	-	-	-0.20	1.23	0.15	-	-	-	0.00	0.04	0.84
e	0.03	2.10	0.02	-	-	-	0.00	0.04	0.46	-	-	-
f	-	-	-	-0.58	1.84	0.44	-	-	-	0.01	0.05	1.67

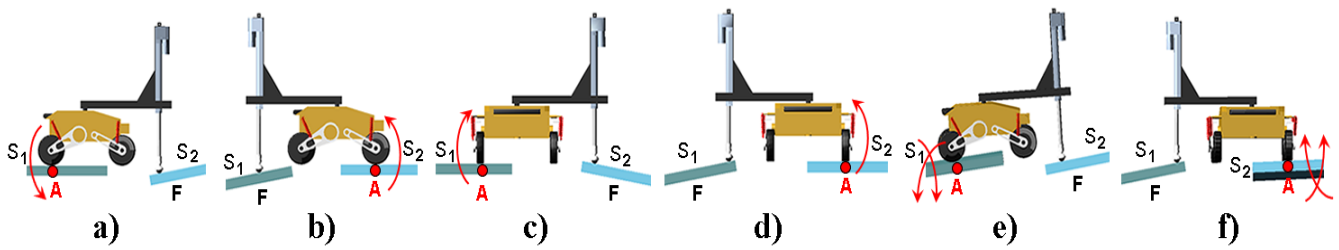

Fig. 13. Simulations to validate I_s with the robot touching the ground at three points

DOI 10.2478/ama-2025-0065

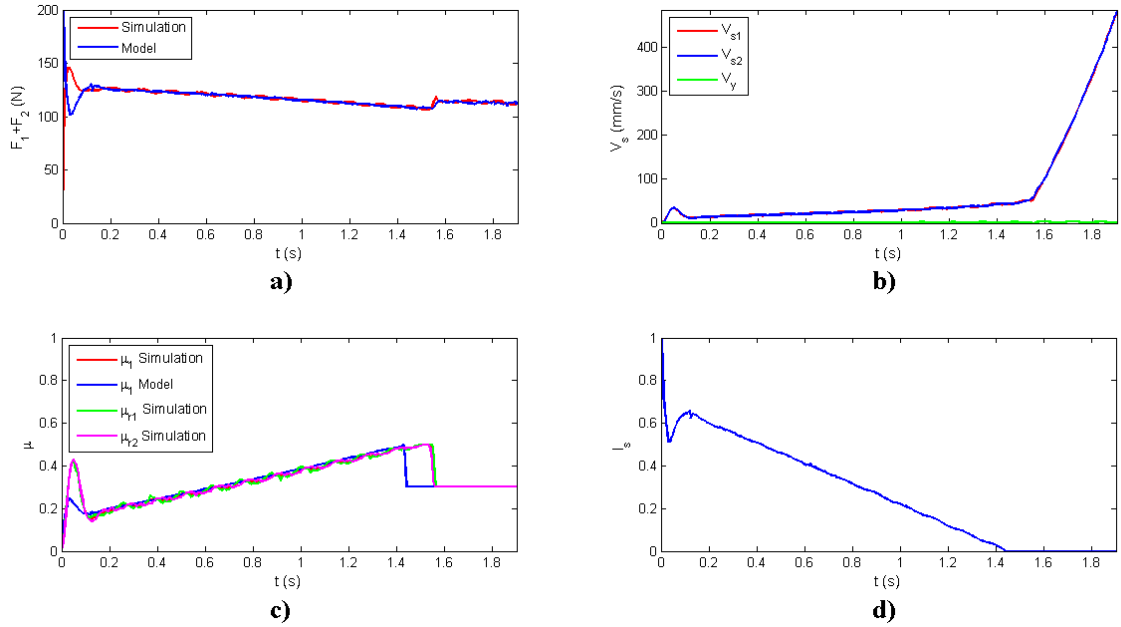

Fig. 14. Results corresponding to Test "b" (see Fig. 13)

3.1.1. Validation of the effectiveness of I_s during obstacle traversal

Although the effectiveness of I_s was verified using MSC. ADAMS while the robot moved on some test surfaces in the previous section, this section describes other tests where the robot is overcoming an obstacle and sliding completely, losing the ability to successfully complete the operation. The purpose of these tests is to verify if in these cases, the previously defined I_s is able to predict such a situation. For this, three simulations (A, B, and C) were performed where the robot executes a strategy to overcome an obstacle, but in this case, the static friction coefficient between the wheels and the surfaces (μ_{s1} and μ_{s2}) was reduced to promote sliding during the simulation. Tab. 4 shows, for each simulation, the geometry of the obstacles and the coefficients μ_{s1} and μ_{s2}.

The results for Simulation A are shown in Fig. 15: the robot begins the obstacle overcoming process and reaches Stage f where the front wheels are positioned on *Surface 2*, and the final elevation of the robot must start due to the action of the second link of the arm that is deployed. In the figure, it can be observed that, at the start of this stage, I_s undergoes a sharp decrease until reaching 0, at the same instant, there are oscillations in the longitudinal (V_x) and transversal (V_y) velocities of the robot since it effectively begins to slide at the time predicted by I_s and moves back, losing its position on the obstacle (as shown in the thumbnail image on Stage F in Fig. 15). The abrupt decrease in I_s is related to the μ_{s2} of *Surface 2*, which is very low ($\mu_{s2} = 0.2$), so when the robot is supported only by the front wheels positioned on this surface, there is not enough grip (no support from the rear wheels), and it begins to slide, a situation predicted by $I_s \approx 0$ at that moment.

Similar results are obtained when studying Simulation B (Fig. 16), where the robot begins the obstacle overcoming process until reaching Stage C where the right-side wheels must be lifted while the second arm link is deployed. At the start of this stage, it is observed that when $F_{5z} > 0$ due to the contact of the arm's end effector with the ground, I_s undergoes a sharp decrease, this time below 0.1, while simultaneously, visible variations occur in the longitudinal velocity (V_x) of the robot as it starts to slide forward. Once again, the abrupt decrease in I_s occurs when the robot is supported only by two wheels on *Surface 1*, which in this case has a $\mu_{s2} = 0.4$, which is not sufficient to provide the necessary grip to two wheels. It is worth noting that in this simulation, I_s did not reach the value of 0 during the moment of sliding, so it is important to avoid $I_s < 0.2$ as a safety condition, which was already explained in the previous section. Next, the results of Simulation C are not shown because they are very similar to those experienced by the robot in Simulation B (the robot also slides in Stage C).

Tab. 4. Geometry of obstacles and static friction coefficients used

Simulation	Description	ϕ_{s1} (°)	α_{s1} (°)	ϕ_{s2} (°)	α_{s2} (°)	γ_{b1} (°)	μ_{s1}	μ_{s2}
A	Frontal ascent	-5.00	0.00	-9.67	-2.58	74.94	1.0	0.2
B	Lateral descent	7.71	0.00	7.50	-4.33	150.22	0.4	0.4
C	Lateral trench	0.00	10.00	0.00	10.00	25.34	0.4	0.4

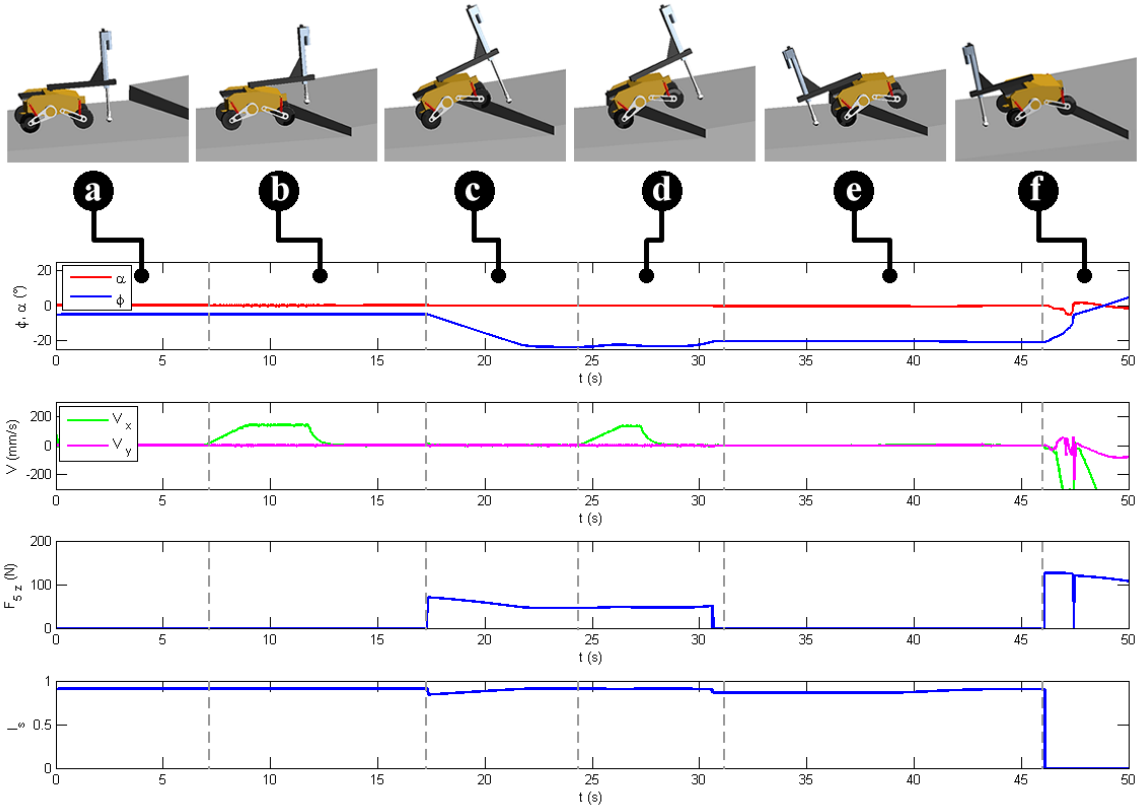

Fig. 15. Analysis of stages for overcoming obstacles until slipping (Simulation A)

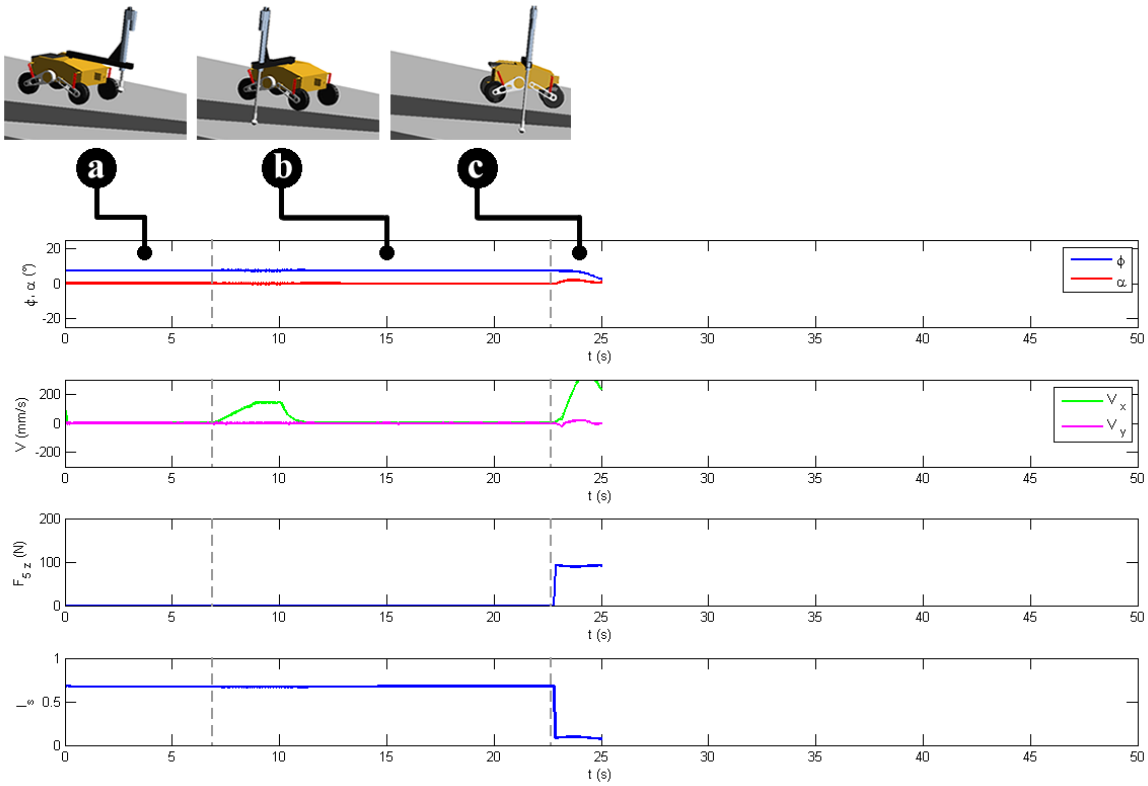

Fig. 16. Analysis of stages for overcoming obstacles until slipping (Simulation B)

DOI 10.2478/ama-2025-0065

3.1. Experimental validation of I_s using the Lázaro robot

Just as the effectiveness of I_s was validated using simulations with MSC. ADAMS, a set of tests was implemented with the Lázaro robot to verify if the proposed I_s can predict the condition of total sliding in the real robot. For this purpose, a test platform was configured as shown in Fig. 17a, where the robot is positioned on two surfaces that can adopt different inclinations (the wheels on the left are on *Surface 1*, while those on the right are on *Surface 2*).

Before starting the tests, it was necessary to determine the static friction coefficient between the surfaces and the robot's wheels; since both surfaces are made of the same material, $\mu_{s1} = \mu_{s2}$. The determination of μ_s was done considering that $\mu_s = \tan \alpha_{c\,lim}$, where $\alpha_{c\,lim}$ is the roll angle of the robot when it, positioned on a single surface with its 4 wheels, starts to slide while $\phi_c = 0$. Upon conducting the corresponding tests, it was found that $\mu_{s1} = \mu_{s2} = 0.522$.

Four tests were designed where *Surface 2* rotated according to the arrow shown in Fig. 17a ($\phi_{s2} = 0°$ and variable α_{s2}), while *Surface 1* remained static, completely horizontal in test "a" ($\phi_{s1} = \alpha_{s1} = 0°$) and with a fixed inclination in the rest of the tests "b - d" ($\phi_{s1} = 0°$ and α_{s1}=-18°). In these experiments, *Surface 2* rotated until the robot started to slide or until the risk of tipping over became significant, necessitating the experiment to be stopped. The results of these 4 tests are shown in Fig. 18, where for each experiment, 3 graphs (arranged vertically) display the angles α_s of *Surfaces 1* and *2*, the angles α_c and ϕ_c of the robot, and the I_s obtained in the test from the previously described theoretical model.

The tests a and d (Fig. 18a and d) show that the obtained I_s never reaches the critical value of 0; therefore, the robot should not slide in these cases, and indeed, during the test, such a situation did not occur. Note that the inclination of the robot in these experiments reached a significant magnitude (test a: $\alpha_c \approx 33°$; test d: $\alpha_c \approx 38°$) and similarly *Surface 2* (test a: $\alpha_{s2} \approx -53°$; test d: $\alpha_{s2} \approx -69°$), but despite this, in neither case did the robot slide as predicted by the calculated I_s. On the contrary, in tests b and c, I_s reaches the value of 0, predicting the sliding, and indeed, in both tests, this phenomenon occurred according to the prediction of I_s.

In test b (Fig. 18b), I_s reaches the value of 0 at around 5 seconds, and almost simultaneously, α_c undergoes a drastic reduction from -33° to -20°, while there is a strong oscillation in ϕ_c. All of this is a consequence of the sliding that occurs in the robot, causing it to descend rapidly until it is completely positioned on *Surface 1*. On the other hand, if we analyze test c (Fig. 18c) where the robot is supported by two wheels plus the end effector of the arm, I_s also reaches the value of 0 at 6 seconds. In this case, the oscillation in α_c and ϕ_c indicating the sliding appears a few moments earlier when $I_s \approx 0.12$, but this is in line with the expected error for this index, reaffirming the established criterion where it is recommended that $I_s \geq 0.2$ to avoid sliding.

4. CONCLUSIONS

The effect of slipping during the obstacle-surmounting process by wheeled mobile robots, especially using an attached arm as a tool for overcoming the obstacle, was estimated. For this purpose, a slipping index was developed, which is a novel metric that quantifies the risk of total slippage. Specifically, this metric allows estimating the moment when the robot loses grip with the ground and starts sliding, deviating from its path and hindering the obstacle-surmounting process. Although this metric was developed for the specific case of a wheeled robot using its arm in contact with the ground as support to overcome the obstacle, it can be extended to other robots that do not have or use their arm in that way, with the condition that the force of contact of the arm with the ground is $F_5 = 0$.

The metric was validated using MSC. ADAMS software, which allows simulating the mechanical model of the robot and the described risk. After conducting these validations, it was found that the proposed model for this index efficiently predicts the intended risk. Furthermore, it was demonstrated that this model generates forecasts with good to high accuracy, as the Mean Absolute Percentage Error (MAPE) between the model and the simulations was consistently low.

The derivation of the slipping index (I_s) was based on the analysis of friction forces between the wheels and the ground. This analysis involved determining δ_n, which is the orientation angle of the friction force on a wheel relative to the X_s axis. To find this angle, a study of multiple typical robot situations facing obstacles was conducted, and δ_n was defined based on these situations. In future research, a more in-depth analysis is needed to determine this angle, especially in situations where the arm exerts force against the ground or where the robot is positioned on an obstacle with surfaces that have very different inclinations from each other, leading to loss of contact with the ground in one of the wheels. It was observed that in these cases, there was the greatest deviation (less than 20%) between the I_s model and the simulation results. Therefore, adjusting the value of δ_n may reduce these errors as it is considered to be the most influential factor in obtaining this divergence.

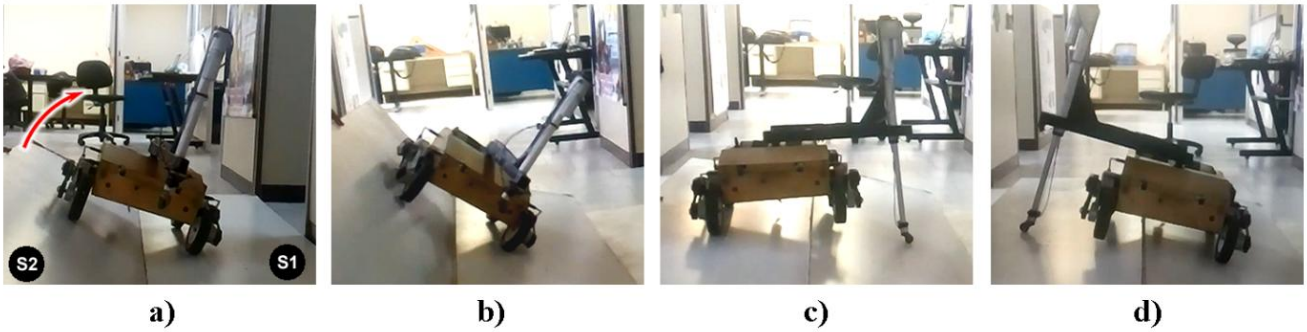

Fig. 17. Tests conducted with the Lázaro robot to validate I_s

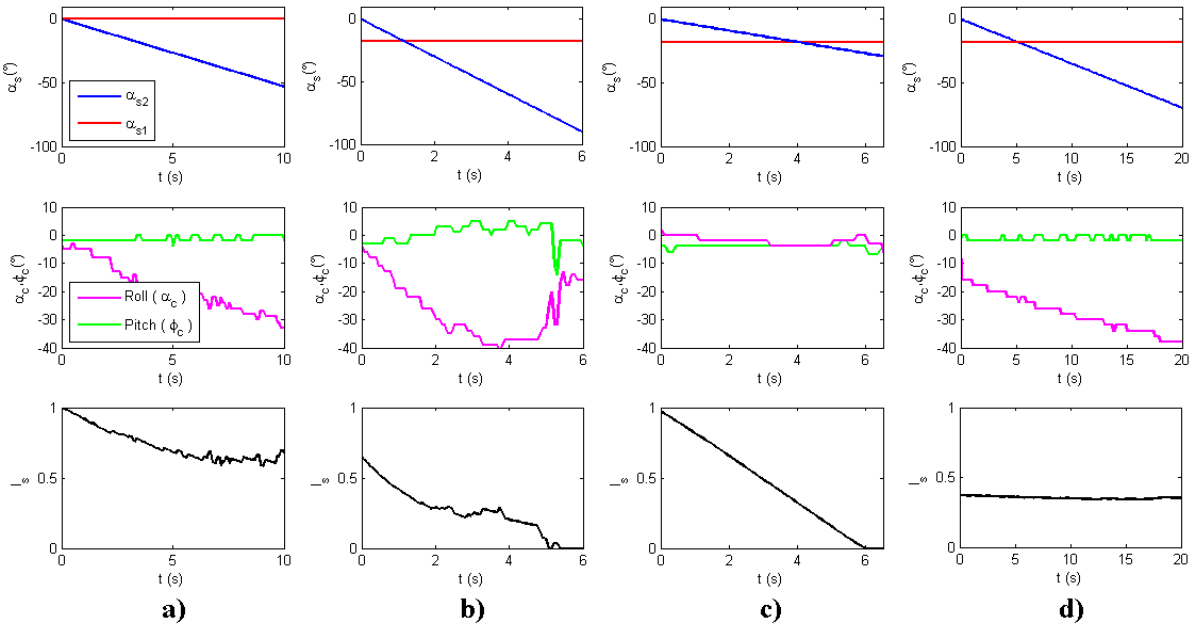

Fig. 18. Results of the tests conducted with the Lázaro robot to validate I_s

REFERENCES

1. Zhang S, Zhao X, Su W, Wu H, Dai Z, Chen Z. The design of suspension mechanism and analysis of obstacle ability to rescue robots. En: Recent Developments in Mechatronics and Intelligent Robotics. ICMIR 2018. Advances in Intelligent Systems and Computing Deng K, Yu Z, Patnaik S, Wang J. Springer; 2018: 677-685.
2. Hadi NH, Younus KK. Path tracking and backstepping control for a wheeled mobile robot (WMR) in a slipping environment. IOP Conference Series: Materials Science and Engineering. 2020; 671: 1-17.
3. Wang Z, Zhao J, Zeng G. Modeling, simulation and implementation of all terrain adaptive five DOF robot. Sensors. 2022; 22(6991): 1-29.
4. Boeder P, Soares C. Mars 2020: mission, science objectives and build. Proc. SPIE 11489, Systems Contamination: Prediction, Control, and Performance. 2020; 11489: 1-17.
5. Bluethmann B, Herrera E, Hulse A, Figuered J, Junkin L, Markee M, et al. An active suspension system for lunar crew mobility. En: IEEE Aerospace ConferenceBig Sky; 2010:1-9.
6. Yehezkel L, Berman S, Zarrouk D. Overcoming obstacles with a reconfigurable robot using reinforcement learning. IEEE Access. 2020; 8: 217541-217553.
7. Song Z, Luo Z, Wei G, Shang J. Design and analysis of a six-wheeled companion robot with mechanical obstacle-overcoming adaptivity. Mechanical Sciences. 2021; 12(2): 1115–1136.
8. Medeiros V, Jelavic E, Bjelonic M, Siegwart R, Meggiolaro M, Hutter m. Trajectory optimization for wheeled-legged quadrupedal robots driving in challenging terrain. IEEE Robotics and Automation Letters. 2020; 5(3): 4172-4179.
9. Huang Y, Meng R, Yu J, Zhao Z, Zhang X. Practical obstacle-overcoming robot with a heterogeneous sensing system: design and experiments. Machines. 2022; 10(289):1-19.
10. Jelavic E, Hutter M. Whole-body motion planning for walking excavators. En: 2019 IEEE/RSJ International Conference on Intelligent Robots and Systems (IROS)Macau. 2019;2292-2299.
11. García JM, Duarte F. Overcoming obstacles with variable geometry and inclination by rolling mobile robots using their arm. Robotica. 2025; 43(5): 1608-1639.
12. Abo-Shanab RF, Sepehri N. Dynamic modeling of tip-over stability of mobile manipulators considering the friction effects. Robotica. 2005; 23(2): 189-196.
13. García JM, Bohórquez A, Valero A. Efecto de la suspensión en el direccionamiento de un robot skid steer moviéndose sobre terrenos duros con diferente rugosidad. Ingenierías USBMed. 2020; 11(1): 18-30.
14. Bevly DM, Ryu J, Gerdes JC. Integrating INS sensors with GPS measurements for continuous estimation of vehicle sideslip, roll, and tire cornering stiffness. IEEE Transactions on intelligent transportation systems. 2006; 7(4): 483-493.
15. Inotsume H, Sutoh M, Nagaoka K, Nagatani K, Yoshida K. Slope traversability analysis of reconfigurable planetary rovers. En: 2012 IEEE/RSJ International Conference on Intelligent Robots and SystemsVilamoura; 2012, 4470-4476.
16. Reina G, Ishigami G, Nagatani K, Yoshida K. Vision-based estimation of slip angle for mobile robots and planetary rovers. En: 2008 IEEE International conference on robotics and automationPasadena; 2008; 486-491.
17. Heverly M, Matthews J, Lin J, Fuller D, Maimone M, Biesiadecki J, et al. Traverse performance characterization for the mars science laboratory rover. Journal of Field Robotics. 2013; 30(6): 835-846.
18. Li W, Gao H, Yang H, Li N, Ding L, Deng Z. A method to online etimate weel's sippage for plnetary rover. En: 11th World congress on intelligent control and automationShenyang. 2014; 2469-2474.
19. Rabiee S, Biswas J. A friction-based kinematic model for skid-steer wheeled mobile robots. En: 2019 International Conference on Robotics and Automation (ICRA)Montreal. 2019; 8563-8569.
20. Ding L, Gao H, Deng Z, Guo J, Liu G. Longitudinal Slip versus skid of planetary rovers' wheels traversing on deformable slopes. En: IEEE/RSJ International Conference on Intelligent Robots and Systems. Tokyo. 2013;2842-2848.
21. Song T, Xi F, Guo S, Tu X, Li X. Slip Analysis for a Wheeled Mobile Manipulator. Journal of Dynamic Systems Measurement and Control. 2018; 140: 1-12.
22. Thueer T, Siegwart R. Mobility evaluation of wheeled all-terrain robots. Robotics and Autonomous Systems. 2010; 58(5): 508-519.
23. García JM, Martínez JL, Mandow A, García-Cerezo A. Slide-Down Prevention for Wheeled Mobile Robots on Slopes. En: 3rd International Conference on Mechatronics and Robotics Engineering Paris. 2017; 1-6.
24. Cholewínski M, Mazur A, Domski W. Preliminary experimental results of factitious force method implementation for the mobile platform REX. En: 21st International Conference on Methods and Models in Automation and Robotics. Szczecin; 2016.
25. Dimastrogiovanni M, Cordes F, Reina G. Terrain sensing for planetary rovers. En: Proceedings of the 3rd IFToMM ITALY Conference. 2020;1-5.
26. Lucet E, Lanain R, Grand C. Dynamic path tracking control of a vehicle on slippery terrain. Control Engineering Practice. 2015; 42: 60-73.

DOI 10.2478/ama-2025-0065

27. Sivaraman D, Pillai BM, Ongwattanakul S, Suthakorn J. Energy optimized path planning and decision making for multiple robots in rescue operations. En: 48th Annual Conference of the IEEE Industrial Electronics Society. 2022;1-6.
28. Wu H, Karkoub M. Frictional forces and torques compensation based cascaded sliding-mode tracking control for an uncertain omnidirectional mobile robot. Measurement and Control. 2022;55(3-4): 178-188.
29. Fiedén M, Bałchanowski J. A mobile robot with omnidirectional tracks—design and experimental research. Applied sciences. 2021; 11(11778): 1-23.
30. Gürgöze G, Türkoglu I. A novel energy consumption model for autonomous mobile robot. Turkish Journal of Electrical Engineering & Computer Sciences. 2022; 30: 216-232.
31. Kim J, Jeong H, Lee D. Performance optimization of a passively articulated mobile robot by minimizing maximum required friction coefficient on rough terrain driving. Mechanism and machine theory. 2021; 164(104368): 1-21.
32. Higashino M, Fujimoto H, Takase Y, Nakamura H. Step climbing control of wheeled robot based on slip ratio taking account of work load shift by anti-dive force of suspensions and accerelation. En: AMC2014Yokohama. 2014;167-172.
33. Bruzzone L, Baggetta M, Nodehi S, Bilancia P, Fanghella P. Functional design of a hybrid leg-wheel-track ground mobile robot. Machines. 2021; 9(10):1-11.
34. Shin J, Son D, Kim Y, Seo T. Design exploration and comparative analysis of tail shape of tri-wheel-based stair-climbing robotic platform. Scientific Reports. 2022; 12(19488): 1-19.
35. Ma J, Cheng J, Zuang D. Analysis of Sojourner's six-wheeled rocker suspension appended with driving moment. En:International Conference on Information Engineering and Computer Science. Wuhan. 2009; 1-4.
36. Bruzzone L, Fanghella P. Functional redesign of Mantis 2.0, a hybrid leg-wheel robot for surveillance and inspection. J Intell Robot Syst. 2016; 81:215–230.
37. Liu Y, Liu G. Track-stair and vehicle-manipulator interaction analysis for tracked mobile manipulators climbing stairs. En: IEEE Conference on Automation Science and Engineering Washington. 2008; 157-162.
38. Li N, Ma S, Li B, Wang M, Wang Y. An online stair-climbing control method for a transformable tracked robot. En: IEEE International conference on Robotics and Automation River Centre. 2012; 923-929.
39. Yu S, Wang T, Wang Y, Zhi D, Yao C, Wang Z, et al. A tip-over and slippage stability criterion for stair- climbing of a wheelchair robot with variable geometry single tracked mechanism. En: IEEE International Conference on Information and Automation Shenyang. 2012; 88-93.
40. Morales J, Martínez J, Mandow A, Serón J, García-Cerezo A, Pequeño-Boter A. Center of gravity estimation and control for a field mobile robot with a heavy manipulator. En: IEEE International Conference on MechatronicsMálaga. 2009; 1-6.
41. Diaz-Calderon A, Kelly A. Development of a terrain adaptive stability prediction system for mass articulating mobile robots. En Yuta S, Asama H, Thrun S, Prassler E, Tsubouchi T. Field and Service Robotics. Berlín: Springer Berlin Heidelberg. 2006; 343-354.
42. Serón J, Martínez JL, Mandow A, García-Cerezo A, Morales J, Reina A, et al. Terrace climbing of the Alacrane mobile robot with cooperation of its onboard arm. En: 12th IEEE International Workshop on Advanced Motion Control Sarajevo. 2012; 1-6.
43. García JM, Medina I, Martínez JL, García-Cerezo A, Linares A, Porras C. Lázaro: Robot Móvil dotado de Brazo para Contacto con el Suelo. Revista Iberoamericana de Automática e Informática Industrial. 2017; 14:174–183.
44. Giesbers J. Contact Mechanics in MSC ADAMS. Bachelor Thesis. Enschede.
45. García JM, Valero A, Bohórquez A. Suspension effect in tip-over stability and steerability of robots moving on terrain discontinuities. Revista Iberoamericana de Automática e Informática Industrial. 2020;17: 202-214.
46. Vivas E, Allende-Cid H, Salas R. A systematic review of statistical and machine learning methods for electrical power forecasting with reported MAPE score. Entropy. 2020; 22(1412):1-24.

This work was partially funded by project No. 01-025-2016 from the Research Dean's Office of the Universidad Nacional Experimental del Táchira.

Jesús M. García: https://orcid.org/0000-0001-5466-9429

Franklyn G. Duarte: https://orcid.org/0009-0009-2143-1436